

RESEARCH ARTICLE

10.1002/2017JA024051

Key Points:

- Applied principal component analysis to TIEGCM simulations and fit resulting modes to Swarm data
- Using a small number of PC modes, we could reproduce EEJ and *Sq* features at low and middle latitudes
- The PCA approach enables prediction of ionospheric fields far from the data region

Correspondence to:

P. Alken,
alken@colorado.edu

Citation:

Alken, P., A. Maute, A. D. Richmond, H. Vanhamäki, and G. D. Egbert (2017), An application of principal component analysis to the interpretation of ionospheric current systems, *J. Geophys. Res. Space Physics*, 122, 5687–5708, doi:10.1002/2017JA024051.

Received 17 FEB 2017

Accepted 2 MAY 2017

Accepted article online 11 MAY 2017

Published online 23 MAY 2017

An application of principal component analysis to the interpretation of ionospheric current systems

P. Alken¹ , A. Maute², A. D. Richmond² , H. Vanhamäki³ , and G. D. Egbert⁴
¹University of Colorado Boulder, Boulder, Colorado, USA, ²High Altitude Observatory, National Center for Atmospheric Research, Boulder, Colorado, USA, ³University of Oulu, Oulu, Finland, ⁴Oregon State University, Corvallis, Oregon, USA

Abstract Ionospheric currents are driven by several different physical processes and exhibit complex spatial and temporal structure. Magnetic field measurements of ionospheric sources are often spatially sparse, causing significant challenges in visualizing current flow at a specific time. Standard methods of fitting equivalent current models to magnetic observations, such as line currents, spherical harmonic analysis, spherical cap harmonic analysis, and spherical elementary current systems (SECS), are often unable to capture the full spatial complexity of the currents or require a large number of parameters which cannot be fully determined by the available data coverage. These methods rely on a set of generic basis functions which contain limited information about the geometries of the various ionospheric sources. In this study, we develop new basis functions for fitting ground and satellite measurements, which are derived from physics-based ionospheric modeling combined with principal component analysis (PCA). The physics-based modeling provides realistic current flow patterns for all of the primary ionospheric sources, including their daily and seasonal variability. The PCA technique extracts the most relevant spatial geometries of the currents from the model run into a small set of equivalent current modes. We fit these modes to magnetic measurements of the Swarm satellite mission at low and middle latitudes and compare the resulting model with independent measurements and with the SECS approach. We find that our PCA method accurately reproduces features of the equatorial electrojet and *Sq* current systems with only 10 modes and can predict ionospheric fields far from the data region.

1. Introduction

Charged particles in the Earth's ionosphere interact with electromagnetic fields, neutral wind frictional forces, gravitational forces, and plasma pressure-gradient forces, resulting in global electrical current flow. Each of the forces acting on the ionospheric plasma, when coupled with the ambient geomagnetic field, produces electric currents which exhibit complex spatial and temporal structure. For *E* region altitudes (90–120 km) at low and middle latitudes, ion-neutral collisions drive much of the plasma motion, while the electrons are largely coupled to the magnetic field lines. Electric fields are generated to ensure that the total current is divergence free. The neutral wind field itself is driven by solar and lunar atmospheric tides, resulting in complex spatial structures which in turn modulate the electric fields and currents in the ionosphere. The large-scale current system at low and middle latitudes resulting from this ion-neutral coupling has been long detected as diurnal variations in ground measurements and is named solar quiet (*Sq*) (see recent review by Yamazaki and Maute [2016]). At the magnetic equator, due to the horizontal geometry of the magnetic field, the effective zonal conductivity, called the Cowling conductivity, experiences an enhancement resulting in significantly increased current flow. This current is called the equatorial electrojet and produces prominent magnetic signatures in both ground and low Earth orbiting (LEO) satellite measurements [Forbes, 1981; Lühr et al., 2004; Alken and Maus, 2007; Yamazaki and Maute, 2016]. Staying at low and middle latitudes, we find interhemispheric field-aligned currents (IHFAC) which are coupled to both the *E* and the *F* regions. These result from the asymmetry in the neutral wind field and conductivity between the Northern and Southern Hemispheres, which can cause a small difference in electric potential between the north/south foot points of a field line, leading to current flow along the field line. Gravitational and pressure-gradient forces acting on ionospheric plasma also cause current flow. These currents are strongest in the low-latitude *F* region, where the

equatorial ionization anomaly peaks and provides a medium for enhanced current flow [Alken, 2016; Alken *et al.*, 2016]. Simulation studies have also found that these current systems produce return current flow through *E* region altitudes [Richmond and Maute, 2014]. At high latitudes, there is strong coupling between processes occurring in the magnetosphere and ionosphere. The solar wind, interacting with the geomagnetic field, traps energetic charged particles in the magnetosphere and drives strong currents. These currents couple to the high-latitude ionosphere, where they form two principal current systems, the polar electrojets (PEJ) in the *E* region and field-aligned currents (FAC) which extend from the ionospheric *E* region up to magnetospheric altitudes. These two current systems are heavily influenced by solar wind behavior and have a much more complex temporal structure than the diurnal current systems in the low- and middle-latitude ionosphere [Olsen and Stolle, 2016].

While the many ionospheric current systems described above are coupled on a global scale through the electromagnetic field, researchers often single out a particular current of interest and develop specialized methods to study its spatial and temporal structure. For data-driven approaches, this is typically done by collecting magnetic field measurements, isolating the perturbation to the total magnetic field caused by the current system of interest and fitting a model of equivalent current flow to the data to attempt to understand the spatial flow patterns and temporal evolution of the current. For physics-based simulation approaches, modelers can turn on and off different source terms in the simulation to isolate the effect of a single current system. In data-driven research, various models have been developed to help understand ionospheric current flow. Line current methods have been applied to satellite observations of the equatorial electrojet [Lühr *et al.*, 2004; Alken *et al.*, 2013, 2014], polar electrojets [Olsen, 1996; Vennerstrom and Moretto, 2013; Aakjær *et al.*, 2016], and gravity currents [Alken, 2016]. Line current methods impose a priori constraints on the current flow direction and are mainly useful for interpreting localized measurements, such as the magnetic observations of a single polar-orbiting satellite or a meridional chain of ground observatories. Since the electrojet flow patterns typically follow lines of constant magnetic latitude, they are well represented by line current geometry. For current systems with more complex spatial geometries, other methods must be used. Spectral methods, such as spherical harmonic analysis (SHA) and spherical cap harmonic analysis (SCHA) are widely used to fit satellite and ground measurements of ionospheric currents. In these methods, magnetic potential functions are expanded in a basis of spherical harmonics or spherical cap harmonics, with unknown coefficients which are determined by fitting to data. SHA is suitable when data are available over a large spatial region and has been used to model *Sq* and *EEJ* currents [Langel *et al.*, 1993; Sabaka *et al.*, 2004; Pedatella *et al.*, 2011; Yamazaki *et al.*, 2011; Chulliat *et al.*, 2013, 2016], high-latitude FAC [Olsen, 1997], and midlatitude IHFAC [Olsen, 1997]. SCHA [Haines, 1985] is useful when observations are available in a localized region (i.e., under a spherical cap of appropriate size) and has been used to study *Sq* [Haines and Torta, 1994] and high-latitude currents [Weimer *et al.*, 2010; Weimer, 2013; Waters *et al.*, 2015]. A different approach called spherical elementary current systems (SECS) was introduced by Amm [1997] and further developed by Amm and Viljanen [1999]. They showed that any 2-D vector field on a sphere, such as current density, can be decomposed as a linear combination of vector basis functions, called elementary currents. These elementary currents are well suited for a spherical geometry and have simple closed form expressions for their magnetic perturbations. SECS can be defined globally or in a localized region, and the amplitudes of the individual elementary systems are determined by fitting to magnetic data.

Line current models, which naturally impose constraints on current flow directions, typically require a modest number of model parameters but are unable to account for spatially complex flow patterns. The SHA, SCHA, and SECS methods are capable of modeling arbitrary spatial complexity in the currents, at the expense of requiring a large number of model parameters. The data available for fitting these models are often limited (i.e., a sparse network of ground observatories or a single satellite track). Therefore, there is a need to devise new methods capable of producing realistic current systems from a sparse set of observations. In this paper, we propose a method of doing this based on a combination of physics-based ionosphere simulations, principal component analysis (PCA), and magnetic measurements from one or more Swarm satellites. The physics-based simulations are designed to model as many ionospheric sources as possible, with realistic day-to-day and seasonal variability. These simulations are then subjected to principal component analysis, which will identify dominant modes of variability, corresponding to significant current flow patterns for the modeled ionospheric sources. These principal component modes will then serve as basis functions for fitting satellite measurements. Since the modes themselves contain the statistically significant current flow patterns as predicted by the physics-based model, it is expected that few modes will be required to explain a given

set of observations, drastically reducing the number of free parameters required in the data fitting. Furthermore, each of the modes will contain spatially complex information, allowing efficient reconstruction of sharp features as seen in the equatorial and polar electrojets, as well as broader large-scale features as seen in S_q currents.

Principal component analysis, also known as empirical orthogonal function analysis, has been used previously to study ionospheric and magnetospheric electrodynamics. *Matsuo et al.* [2002, 2005] used a PCA method to study high-latitude electric fields based on ion drift measurements from the Dynamics Explorer 2 and DMSP satellites and the Super Dual Auroral Radar Network (SuperDARN). *Cousins et al.* [2013] further studied principal component modes of electric fields using SuperDARN data, while *Cousins et al.* [2015] used PCA to study spatial patterns of high-latitude electric and magnetic potential based on SuperDARN and AMPERE data. Several studies have developed PCA methods to use external field variations to probe solid Earth conductivity structure [Egbert and Booker, 1989; Egbert, 1997; Smirnov and Egbert, 2012]. *Sun et al.* [1998] used a PCA method to study ionospheric equivalent currents using a ground observatory network. In all of these studies, PCA was applied to a spatially distributed set of observations. In this study, for the first time we will apply principal component analysis to the output of a sophisticated ionosphere electrodynamics physics-based model and use the resulting spatial modes to fit magnetic observations from the Swarm satellite constellation.

1.1. Swarm Satellite Data

Swarm is a low Earth orbiting (LEO) mission [Friis-Christensen et al., 2006], composed of three satellites named A, B, and C which were launched in November 2013. Each satellite flies in a near-polar orbit with inclinations of 87.4° for A and C and an inclination of 88° for B. Each satellite carries a vector fluxgate magnetometer (VFM) mounted next to a three-head star camera which provides attitude information to transform the vector measurement into a geographic north-east-center (NEC) frame. Additionally, each satellite carries an absolute scalar magnetometer (ASM) [Leger et al., 2009] which provides an absolute calibration of the fluxgate instrument. A lower pair of satellites (A and C) fly at about 450 km altitude in a side-by-side constellation separated by about 1.4° longitude at the equator, while B flies higher near 530 km and whose orbital plane slowly drifts from that of A and C. The constellation of three satellites allows measurements of the large-scale ionospheric currents in different local time sectors, which we will exploit for fitting our spatial modes derived from the physics-based modeling.

Swarm C no longer has a functioning ASM after 5 November 2014 due to instrument failure [Fratter et al., 2016], and so after this date, its VFM is calibrated by mapping the scalar field measurement from Swarm A. Additionally, on all three Swarm satellites differences between the ASM measurement and the modulus of the VFM were detected shortly after launch [Lesur et al., 2015]. These differences were found to be related to Sun incidence angles though the root cause of the effect is still unknown. A model, called dB_Sun, was developed to correct for this effect, which is detailed in Tøffner-Clausen et al. [2016]. In this paper, we use Swarm data from baseline 0408 and 0409 for our analysis, which has been corrected for the dB_Sun effect and includes the Swarm C VFM data cross calibrated using Swarm A.

1.2. TIEGCM Physics-Based Modeling

In this study we use the Thermosphere-Ionosphere-Electrodynamic General Circulation Model (TIEGCM) [Roble et al., 1982, 1988; Richmond et al., 1992] to produce time series of global maps of ionospheric equivalent currents. These maps will then serve as the inputs for principal component analysis in order to determine the dominant modes of spatial variability in the ionosphere. TIEGCM is a 3-D physics-based model of the coupled thermosphere-ionosphere region from 97 to 600 km altitude. The model simulates the dynamics, electrodynamics, and chemical interactions within the thermosphere-ionosphere region, as well as its coupling to the mesosphere below and the magnetosphere above [Qian et al., 2014]. The ionospheric electrodynamic solver in TIEGCM simulates all source terms, including the neutral wind dynamo, gravity and plasma pressure-gradient currents, and high-latitude magnetospheric energy input [Richmond and Maute, 2014].

The simulation approach used in the present study is described by Maute [2017], and the main points are briefly summarized here. The lower boundary of the TIEGCM (approximately at 97 km) is defined by the thermosphere-ionosphere-mesosphere electrodynamic GCM simulations described by Häusler et al. [2015], which include realistic tidal and wave variability as represented by the Modern-Era Retrospective Analysis for Research and Applications (MERRA) reanalysis data. Monthly climatological background (i.e., zonal and diurnal mean values) at the lower boundary is defined by empirical models [e.g., Jones et al., 2014; Maute, 2017]. At high

latitudes the magnetosphere-ionosphere coupling is defined by empirical ion convection [Heelis et al., 1982] and auroral particle precipitation patterns which are parameterized by the K_p index [Emery et al., 2012]. TIEGCM solves for the unknown global electrostatic potential by requiring that the total current is divergence free. Once the electrostatic potential is determined, the full 3-D current can be recovered. In this study, however, we use a simplified representation of the ionospheric currents, composed of a 2-D horizontal current sheet at 110 km altitude, connected with FAC above, as described by Richmond and Maute [2014]. This approach is well suited to study the structures of currents whose horizontal extent is much greater than vertical, such as Sq , equatorial and polar electrojet zonal currents, and gravity currents. To characterize currents which exhibit poloidal flow, such as pressure-gradient currents, high-latitude FAC, and equatorial electrojet meridional currents, we would need to use the full 3-D TIEGCM current. In this paper, we will restrict our analysis to toroidal current systems at low and middle latitudes, primarily Sq and EEJ, and postpone analysis of the poloidal and high-latitude current systems to a future study.

1.3. Principal Component Analysis

Principal component analysis is useful for quantifying the relationship between a set of interrelated variables. Consider a set of N sensors measuring some physical phenomenon. Unless the physical system under study is extremely simple, or the experimenters have a priori knowledge of where to best locate the sensors, it is likely that the sensor placement is not optimal. In the resulting data set, this would cause intercorrelations between data measured by different sensors, indicating that some of the data are redundant and not useful for adding understanding to the physics of the system. The purpose of principal component analysis is to find linear combinations of the data measured by the N sensors which (1) are uncorrelated with each other and (2) maximize the variance explained in the data. In practice, this is accomplished by constructing the covariance matrix of all the sensor data and diagonalizing it. The covariance matrix contains all the linear dependencies between each pair of sensors, and the diagonalization process finds a basis of eigenvectors which are linear combinations of the original sensor inputs that satisfy the two criteria above. Since the covariance matrix is diagonal in this new basis, the eigenvectors are by definition uncorrelated with each other. Furthermore, the eigenvalues which form the diagonal entries of the covariance matrix represent exactly the amount of variance explained by each eigenvector. Therefore, the eigenvectors are typically sorted from largest to smallest eigenvalue and called principal components (PC). The PC corresponding to the largest eigenvalue will explain the most variance in the data and so on, down to the smallest eigenvalue. The PCs corresponding to the smaller eigenvalues will add little new understanding of the data and represent the “redundant information” discussed above. They can usually be safely discarded from the analysis. PCA is thus used to reduce the dimensionality of the original data set and find an optimal basis for analyzing the particular system under study.

In this work, we are interested in analyzing ionospheric current systems as measured by satellite magnetic measurements during a single orbit. But due to the sparse availability of the satellite data during one orbit, and the large spatial complexity of the ionospheric currents, we wish to construct a small set of basis functions, which capture the primary ionospheric flow patterns, that we can fit to the satellite data. In this application, the “sensors” discussed above represent sampling of ionospheric current simulations provided by TIEGCM. As described by Richmond and Maute [2014], the 3-D current within and above the ionosphere is first represented as a 2-D current sheet at 110 km connected with FAC above. The magnetic perturbations of this sheet-current-plus-FAC are then calculated and used to determine an equivalent toroidal current sheet at 110 km that would produce the same magnetic perturbations at the ground, though not at LEO satellite altitude. In addition to this equivalent current, there is a divergent horizontal current at 110 km plus the FAC, which together produce no magnetic perturbation on the ground, though they do produce magnetic effects at LEO. For the present study we use only the toroidal equivalent current, which contains the main effects of the electrojets and of Sq currents, to calculate magnetic perturbations above 110 km, recognizing that satellite magnetometers would also register effects we neglect associated with the FAC and with poloidal pressure-gradient ionospheric currents. In the future, our method could be extended to include magnetic effects of the FAC and other poloidal currents.

Once we have time series of the 2-D equivalent current sheet on a spherical shell in the E region, we can proceed in several ways. We could define each grid point as a sensor which measures a time series of simulated data at one location and form a covariance matrix of the time series measured by all grid points. However, due to the sharp spatial resolution of the electrojets, we use grids with a spacing of 2° in latitude and 5° in longitude, for a total of 6643 grid points. Additionally, there are two components of the horizontal current at each grid point, making a total of 13286 sensors. In order to reduce the number of sensors, we can recognize that

equivalent current flowing on a spherical shell can be more compactly represented by a spherical harmonic expansion of a single scalar function. In order to represent the sharp spatial features of the electrojets, we found that an expansion to spherical harmonic degree 60 and order 30 is sufficient to fully capture the ionospheric spatial variations. Now we can define our sensors as the spherical harmonic coefficients themselves, leading to a total of 2790 sensors. In this way we preserve nearly all the information of the equivalent current flow at each time step but only need to diagonalize a 2790×2790 covariance matrix. The eigenvectors, or PC modes, of the covariance matrix will represent linear combinations of the spherical harmonic coefficients which best capture the variability of the ionospheric equivalent currents. These modes can then be used to construct a set of equivalent current maps which can be fitted to the magnetic measurements of the Swarm data. Due to the redundant information present in the spherical harmonic representation, we will require far fewer than 2790 modes for the data fitting.

1.4. Spherical Elementary Current Systems

The Helmholtz theorem of vector calculus states that a sufficiently smooth vector field in three dimensions can be decomposed as the sum of a curl-free vector field and a divergence-free vector field. The spherical elementary current system (SECS) approach takes this one step further to decompose each of these two vector fields into sums of curl-free and divergence-free “elementary” vector fields in a spherical coordinate system. These elementary vector fields, also called current systems, form a complete basis to decompose an arbitrary vector field, such as ionospheric current density. The SECS approach has been widely applied to constructing ionospheric equivalent current at high latitudes [Amm and Viljanen, 1999; Pulkkinen et al., 2003; Vanhamäki et al., 2003; Juusola et al., 2006]. Furthermore, the SECS decomposition can be applied also to the electric field, which allows a technique of recovering both ionospheric current and conductance from combined magnetic and electric field measurements [Amm et al., 2015; Juusola et al., 2016]. The SECS method has found only limited application to current systems at low and middle latitudes [Deguchi et al., 2013], which are the subject of this study. We could have chosen a spherical harmonic method to compare with our new PCA approach, but we chose SECS for a few reasons. First, it is easily implemented as a local method, suitable for fitting data from two or three Swarm satellite tracks. Second, there exists a 1-D variant which is designed for fitting single satellite data by assuming vanishing longitudinal gradients. The SECS method also has a few other attractive properties which are discussed further in section 2.2.

2. Methodology

2.1. TIEGCM and PCA

We performed a simulation of TIEGCM from 10 January to 31 December 2009, a total of 355 days. This time period corresponds to low geomagnetic activity and solar flux levels (average $F_{10.7} = 70.6$ solar flux units). For each time step, we computed an equivalent current function as described by Richmond and Maute [2014], projected onto a spherical shell at 110 km altitude, representing the equivalent toroidal current flow in the E region. In general, a toroidal current density field $\mathbf{J}(\mathbf{r}, t)$ can be represented at a location \mathbf{r} and time t as

$$\mu_0 \mathbf{J}(\mathbf{r}, t) = \mathbf{r} \times \nabla Q(\mathbf{r}, t) \quad (1)$$

for some scalar function $Q(\mathbf{r}, t)$, where μ_0 is the magnetic permeability of free space. $Q(\mathbf{r}, t)$ can be expanded in a basis of spherical harmonics as

$$Q(\mathbf{r}, t) = \frac{1}{R} \sum_{nm} Q_{nm}(r, t) Y_{nm}(\theta, \phi) \quad (2)$$

where n is summed from 1 to N , m is summed from $-\min(n, M)$ to $+\min(n, M)$, r is radial distance, θ is geocentric colatitude, and ϕ is longitude, and

$$Y_{nm}(\theta, \phi) = \begin{cases} S_{nm}(\cos \theta) \cos(m\phi) & m \geq 0 \\ S_{n|m|}(\cos \theta) \sin(|m|\phi) & m < 0 \end{cases} \quad (3)$$

Here $S_{nm}(\cos \theta)$ are the Schmidt-normalized associated Legendre functions and $R = 6371.2$ km is a reference radius used so that $Q_{nm}(r, t)$ will have units of magnetic field. We choose $N = 60$ and $M = 30$ which is adequate to capture the sharp features of the electrojets. If we restrict current flow to a spherical shell at radius $r = b$, then we may use the Dirac delta function to define a new set of coefficients $q_{nm}(t)$ which describe the current flow on the shell, independent of radius:

$$Q_{nm}(r, t) = q_{nm}(t) b \delta(r - b). \quad (4)$$

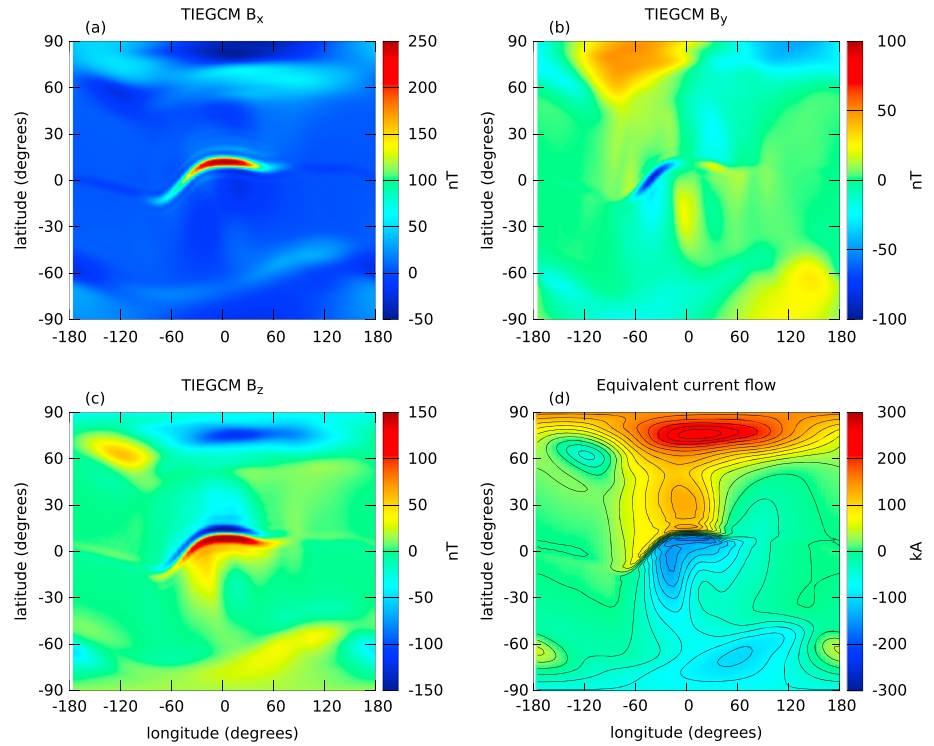


Figure 1. (a–c) Snapshot surface maps of ionospheric field magnetic perturbations produced from TIEGCM model on 25 April 2009 12:00:00 UTC. B_x , B_y , and B_z components are plotted in NEC frame. (d) Current stream function χ , representing equivalent current flow on a spherical shell at 110 km altitude which corresponds to the magnetic perturbations shown.

Defining a toroidal sheet current density $\mathbf{K}(\theta, \phi, t)$ flowing on a shell $r = b$ through the relation $\mathbf{J}(\mathbf{r}, t) = \delta(r - b)\mathbf{K}(\theta, \phi, t)$, we find

$$\mathbf{K}(\theta, \phi, t) = \nabla \times [\hat{\mathbf{r}}\chi(\theta, \phi, t)], \quad (5)$$

where $\hat{\mathbf{r}}$ is the radial unit vector and the *current stream function* χ is given by

$$\chi(\theta, \phi, t) = -\frac{b}{\mu_0} \sum_{nm} q_{nm}(t) Y_{nm}(\theta, \phi). \quad (6)$$

Here the current density $\mathbf{J}(\mathbf{r}, t)$ has units of A/m², while the vector field $\mathbf{K}(\theta, \phi, t)$ represents height-integrated current and has units of A/m. The stream function χ has units of ampere. The radius of the equivalent current shell is set to $b = R + 110$ km. The current stream function $\chi(\theta, \phi, t)$ is computed at each time step from the equivalent current $\mathbf{K}(\theta, \phi, t)$ output by TIEGCM using a spherical harmonic decomposition as described in *Richmond and Maute [2014]*. The maximum spherical harmonic degree $N = 60$ and order $M = 30$ results in a total of 2790 coefficients $q_{nm}(t)$. All equivalent current maps in this paper will show the function χ and its contours. Current flow will follow the contours of χ , counterclockwise around a maximum and clockwise around a minimum. With the $q_{nm}(t)$ determined from the TIEGCM maps, the corresponding magnetic field can be calculated for $r > b$ above the current shell (i.e., at satellite altitude) as

$$\begin{pmatrix} B_r \\ B_\theta \\ B_\phi \end{pmatrix}(\mathbf{r}, t) = -\frac{b}{R} \sum_{nm} \frac{n}{2n+1} q_{nm}(t) \left(\frac{b}{r}\right)^{n+2} \begin{pmatrix} (n+1)Y_{nm}(\theta, \phi) \\ -\partial_\theta Y_{nm}(\theta, \phi) \\ -\frac{1}{\sin\theta} \partial_\phi Y_{nm}(\theta, \phi) \end{pmatrix}. \quad (7)$$

Figure 1 shows a snapshot of the TIEGCM output for 12 UT on 25 April 2009. Figures 1a–1c depict the NEC frame X (northward, $-B_\theta$), Y (eastward, B_ϕ), and Z (center, $-B_r$) components of the ionospheric magnetic field at the Earth's surface, while Figure 1d shows the current stream function χ and equivalent current flow at 110 km altitude.

Figure 2 shows time series for the first few $q_{nm}(t)$ during February 2009. We see clearly the diurnal variations in each time series. The spikes occurring on the 4th, 14th, and 23rd of the month are likely due to increased

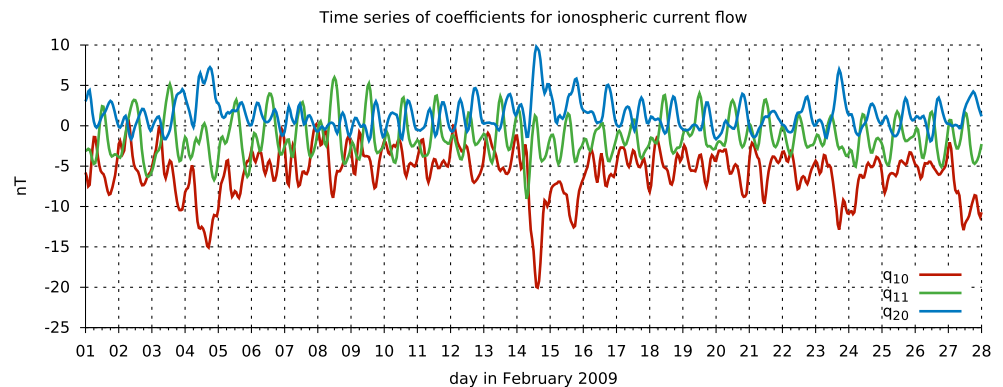


Figure 2. Time series for $q_{10}(t)$ (red), $q_{11}(t)$ (green), and $q_{20}(t)$ (blue) for month of February 2009.

geomagnetic activity, when the Kp index reached 4−, 4+, and 3o, respectively. Also, we can see an anticorrelation between $q_{10}(t)$ and $q_{20}(t)$. In fact, significant statistical correlations exist between many pairs of the spherical harmonic time series. This indicates that by parameterizing the ionospheric currents with spherical harmonics, we necessarily must accept that there exists redundant information among the 2790 spherical harmonic parameters. This is largely due to the fact that the ionospheric current structure is heavily aligned with the geomagnetic field, while the spherical harmonics contain no information about the geomagnetic geometry. Therefore, we must use a large number of spherical harmonic parameters to capture this complex geometry. This is not necessarily problematic for analyzing TIEGCM model runs, which produce global maps of the ionospheric currents, but if we wish to understand the ionospheric current signatures present in a sparse data set of satellite and/or ground observations, the large number of parameters required for a spherical harmonic decomposition becomes prohibitively difficult.

Our goal is to find a method of parameterizing the ionospheric currents in a way which will reduce the number of free parameters while at the same time captures as much of the spatial geometry as possible. One approach would be to switch from spherical harmonics to harmonics in quasi-dipole (QD) coordinates [Richmond, 1995] which by their definition are aligned with the geomagnetic main field geometry. This approach has been used extensively, for example, in the Comprehensive Model [Sabaka et al., 2004, 2013] and the Swarm Level-2 ionospheric field product [Chulliat et al., 2013, 2016]. However, quasi-dipole harmonics are defined only with respect to a geomagnetic main field model and still require many coefficients in order to represent ionospheric field geometries, which are much more complex than the main field. For example, the Dedicated Ionospheric Field Inversion Swarm Level-2 product [Chulliat et al., 2013, 2016], which aims only to model the ionospheric midlatitude Sq system and its induced counterpart, uses a QD harmonic expansion to degree 45 and order 5, for a total of 475 parameters [Chulliat et al., 2013].

We believe that the number of required parameters can be lowered significantly by using a specialized basis which accounts for the geometry of each ionospheric source. To construct such a basis, we will apply principal component analysis (PCA) to the spherical harmonic time series derived above from the TIEGCM model runs. The main idea is instead of using spherical harmonics, which contain statistical correlations among the different parameters as discussed previously, we wish to find linear combinations of the spherical harmonic parameters which will be statistically independent. These linear combinations will be called modes and will arise as the eigenvectors of the covariance matrix of all the spherical harmonic time series. Since the low- and middle-latitude ionospheric currents are heavily aligned with day/night differences, we divide the TIEGCM maps into 1 h universal time (UT) bins and analyze each UT bin separately to avoid mixing day and nighttime current effects at the same longitude in our resulting PC maps. Such a separation may not be necessary for studying the strong daytime E region currents but would likely be needed to model the weaker nighttime and F region currents. First, we center each $q_{nm}(t)$ time series by subtracting its mean value over the full model time span. This is a standard step when calculating covariances between different time series. Then, for each integer UT hour $h \in [0, 23]$, we collect all centered $q_{nm}(t)$ values corresponding to that UT hour:

$$\xi_{nm}^{(h)}(t) = \{q_{nm}(t) - \overline{q_{nm}} : t \text{ corresponds to } h \text{ UT}\}, \quad (8)$$

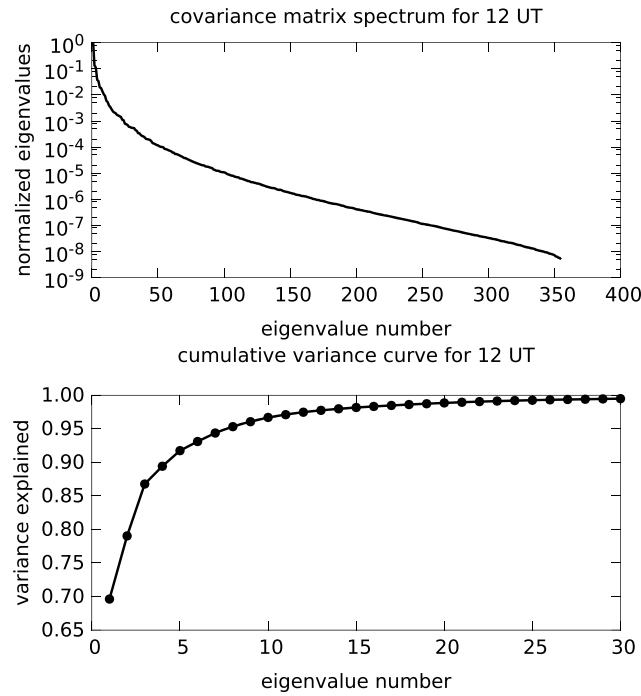


Figure 3. (top) Eigenvalue spectrum of covariance matrix for 12 UT bin, normalized by the largest eigenvalue. (bottom) Cumulative variance explained by eigenvectors also for 12 UT, plotted versus eigenvalue number for first 30 eigenvalues.

where $\overline{q_{nm}}$ is the mean value of $q_{nm}(t)$. Since we are using a 355 day TIEGCM run with 1 h time steps, on each day we will obtain a value of $\xi_{nm}^{(h)}$ for each $h \in [0, 23]$. Therefore, each time series $\xi_{nm}^{(h)}(t)$ will contain $N_t = 355$ samples, or one sample per day for the full time span, where the sample for each day corresponds to h UT. Next, for each UT bin, we define a 2790-by- N_t matrix $X(h)$, whose rows are the binned, centered time series indexed by n, m , and whose columns represent the N_t samples for each day during the year. The matrices $X(h)$ are defined by

$$X(h) = \begin{pmatrix} \xi_{1,-1}^{(h)} \\ \xi_{1,0}^{(h)} \\ \xi_{1,1}^{(h)} \\ \vdots \\ \xi_{60,-30}^{(h)} \\ \vdots \\ \xi_{60,30}^{(h)} \end{pmatrix}, \quad (9)$$

where $\xi_{nm}^{(h)}$ is a row vector consisting of the 355 samples $\xi_{nm}^{(h)}(t)$. The covariance matrix for UT hour h is then given by

$$C(h) = \frac{1}{N_t} X(h) X(h)^T. \quad (10)$$

By constructing this outer product, we are simply taking each pair of centered time series, multiplying point-wise and summing, which is the definition of covariance. The factor of $1/N_t$ in front acts as a weighting term, assigning equal weight to each part of the time series. In principle, we could adjust this term in order to upweight or downweight different time periods of the TIEGCM model run.

The next step after constructing the covariance matrix $C(h)$ is to diagonalize it. Because the spherical harmonic representation of the ionospheric currents is not optimal (i.e., there are statistical correlations among the different parameters), the matrix $C(h)$ will be dense. By diagonalizing $C(h)$, we are constructing a new basis of eigenvectors, or modes, which are statistically independent from each other. Furthermore, the eigenvalues which are the diagonal elements of the new covariance matrix, represent the variance in the TIEGCM output explained by each eigenvector. The eigenvector corresponding to the largest eigenvalue will explain the most variance, followed by the second and so on. Figure 3 (top) shows the eigenvalue spectrum of $C(h)$, normalized by the largest eigenvalue, for $h = 12$ UT. We see that the eigenvalues span roughly 10 orders of magnitude. In practice, the modes corresponding to a few of the largest eigenvalues are all that are needed to explain most of the variance in the ionospheric current output of TIEGCM. The modes corresponding to the tiny eigenvalues contribute almost no relevant information to our understanding of the ionospheric geometry. This can be further seen in Figure 3 (bottom), which shows the cumulative variance curve of the eigenvalues, also for 12 UT. Denoting the eigenvalues by λ_i and ordering them from largest to smallest, the cumulative variance of eigenvalue i is defined as

$$\sigma_i^2 = \frac{\sum_{j=1}^i \lambda_j}{\sum_{j=1}^P \lambda_j}, \quad (11)$$

where $P = 2790$ is the total number of eigenvalues of $C(h)$. From the cumulative variance curve, we compute that it takes 22 eigenmodes to explain more than 99% of the variance of the TIEGCM model run for the 12 UT bin. This is a drastic reduction from the original 2790 spherical harmonic basis functions, but in practice when fitting satellite data, we do not even need to use that many modes. We have found that we can achieve meaningful fits with only about 10 modes. This will be discussed further in section 3.

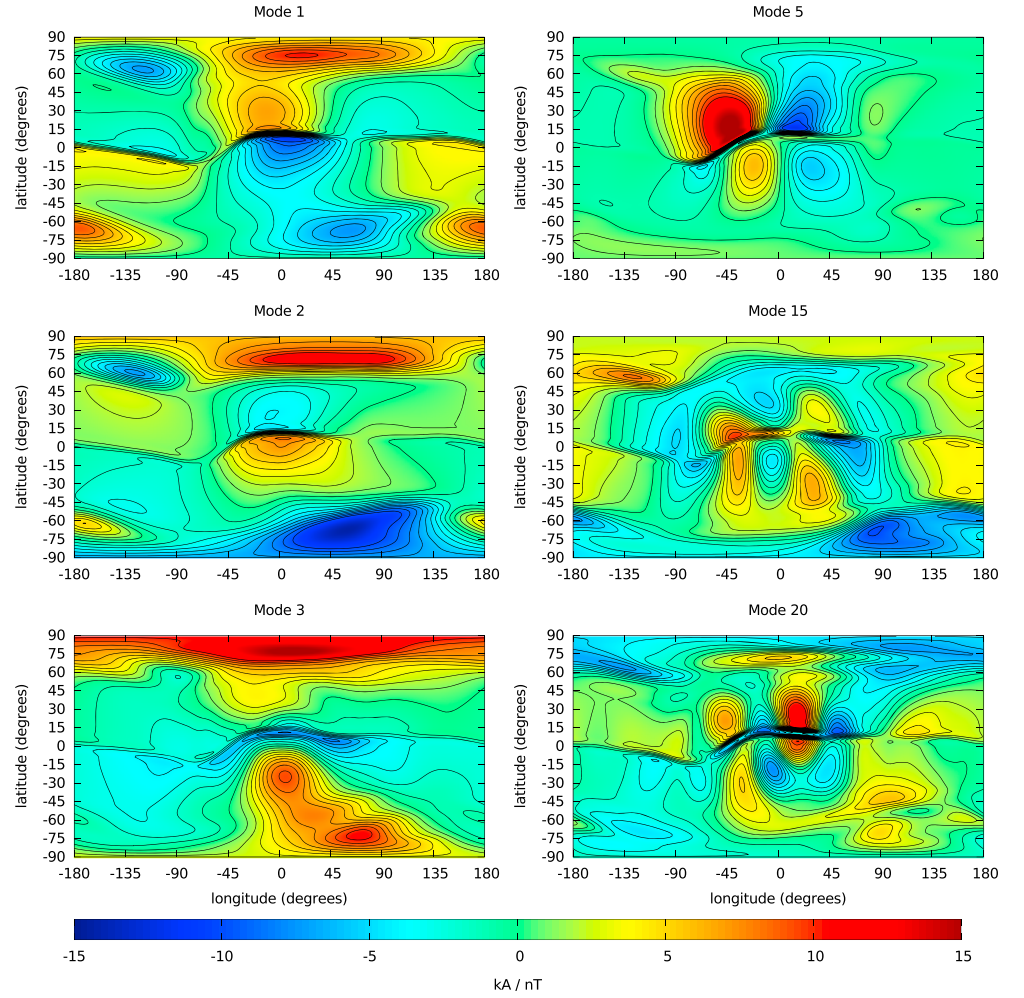


Figure 4. Eigenmodes of TIEGCM-derived covariance matrix for 12 UT visualized as equivalent current maps at 110 km altitude. Modes 1, 2, 3, 5, 15, and 20 are shown.

Figure 4 plots a few of the eigenmodes for 12 UT as equivalent current sheets at 110 km altitude in the *E* region ionosphere. The modes are plotted using their equivalent current stream functions, defined for mode *p* as

$$\chi_p(h, \theta, \phi) = -\frac{b}{\mu_0} \frac{b}{R} \sum_{nm} \hat{\xi}_{nm}^{(h)}(p) Y_{nm}(\theta, \phi), \quad (12)$$

where $\hat{\xi}_{nm}^{(h)}(p)$ represents the elements of the *p*th eigenvector of the covariance matrix *C*(*h*). Similarly to equation (7), the magnetic field for the *p*th principal component for *r* > *b* is

$$\mathbf{B}_p(h, \mathbf{r}) = -\frac{b}{R} \sum_{nm} \frac{n}{2n+1} \hat{\xi}_{nm}^{(h)}(p) \left(\frac{b}{r}\right)^{n+2} \begin{pmatrix} (n+1)Y_{nm}(\theta, \phi) \\ -\partial_\theta Y_{nm}(\theta, \phi) \\ -\frac{1}{\sin \theta} \partial_\phi Y_{nm}(\theta, \phi) \end{pmatrix}, \quad (13)$$

where as before components are ordered in the *r*, *θ*, *φ* basis.

Figure 4 plots contours of the current stream functions $\chi_p(h, \theta, \phi)$ for *p* = 1, 2, 3, 5, 15, 20 and *h* = 12 UT. We can see that each mode exhibits the geometry of the magnetic equator at low latitudes, giving us an efficient means of reconstructing the equatorial electrojet and *Sq* current systems. The high-latitude patterns represent geometries of the polar electrojets, although we will focus on the low and middle latitudes for fitting satellite data in this study. We also see that the longitudinal spatial patterns exhibit increasingly complex structure for higher modes. Figure 5 plots contours of $\chi_p(h, \theta, \phi)$ for the same modes but with *h* = 15 UT. At 15 UT,

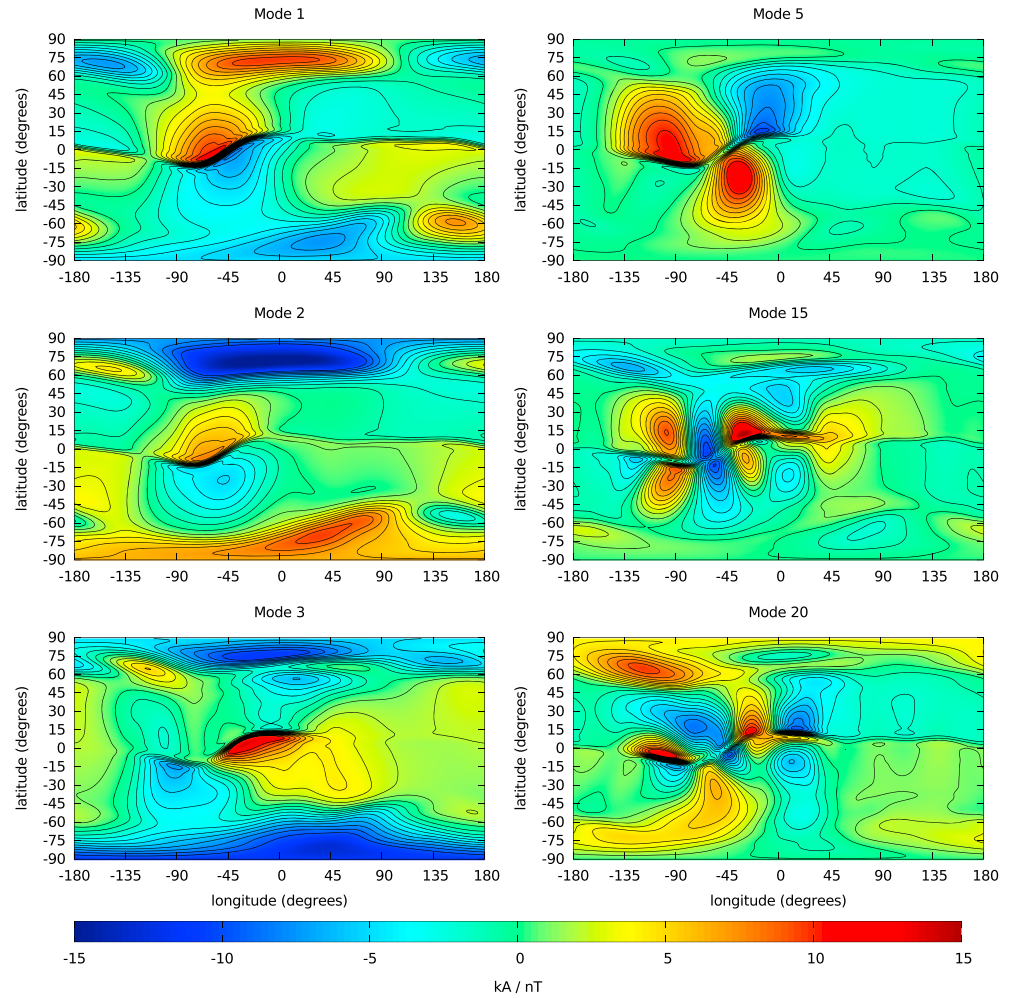


Figure 5. Eigenmodes of TIEGCM-derived covariance matrix for 15 UT visualized as equivalent current maps at 110 km altitude. Modes 1, 2, 3, 5, 15, and 20 are shown.

the *Sq* and EEJ current systems are centered in the South American sector where the magnetic equator diverts southward. We see this geometry clearly in the equivalent current maps, which will help greatly when fitting satellite data in that longitude sector.

When fitting satellite data, we will model the satellite measurements as

$$\mathbf{B}(\mathbf{r}_i, t_i) = \sum_{p=1}^P \alpha_p \mathbf{B}_p(h_i, \mathbf{r}_i), \quad (14)$$

where \mathbf{r}_i and t_i are the position and time of the satellite measurement, respectively, h_i is the UT hour corresponding to the measurement time t_i , P is the number of principal components used in the model, α_p is the coefficient for the p th principal component, and $\mathbf{B}(\mathbf{r}_i, t_i)$ is the ionospheric field perturbation as measured by the satellite. We will discuss the preprocessing method used to isolate the ionospheric field contribution $\mathbf{B}(\mathbf{r}_i, t_i)$ from the total field measurement in section 3. For now we may assume that we have T total vector measurements (from either a single or multiple satellites) and form a vector of observations \mathbf{y}_{obs} of length $3T$. Next, we form a $3T$ -by- P matrix H relating the model coefficients α_p to the observations by

$$H(3i : 3i + 2, j) = \mathbf{B}_j(h_i; \mathbf{r}_i), \quad (15)$$

where the above notation indicates that the three rows of H indexed by $3i, 3i + 1, 3i + 2$ contain the magnetic field vector on the right-hand side for each of the modes $j = 1, \dots, P$. Then we will have

$$\mathbf{y}_{\text{obs}} \approx H\alpha. \quad (16)$$

This equation could be solved for the unknown model coefficients α using typical least squares methods with regularization. However, since we have an estimate of the full model covariance, it is natural to use the method of optimal interpolation, which, in principle, can provide the best linear unbiased estimate of the magnetic fields. Optimal interpolation (OI), which has been used previously to study ionospheric dynamics [Richmond and Kamide, 1988; Matsuo et al., 2005; Cousins et al., 2013, 2015], combines the data and model covariances to obtain a solution for α by solving the following optimization problem:

$$\min_{\alpha} (\mathbf{y}_{\text{obs}} - H\alpha)^T R^{-1} (\mathbf{y}_{\text{obs}} - H\alpha) + \alpha^T \tilde{C}^{-1} \alpha. \quad (17)$$

Here R is the observational error covariance matrix, \tilde{C} is the (diagonal) model error covariance matrix (i.e., $C(h)$ expressed in the basis of eigenmodes for a given UT h), and the other parameters are defined above. Some authors first remove a background model from the observations prior to solving the above minimization problem, in which case the model parameters α will represent deviations from the average background. We could, in principle, do this, as there does exist a climatological ionospheric Sq model as a Swarm Level-2 product [Chulliat et al., 2013, 2016]; however, for this study we will directly fit the PC modes to the full ionospheric field observations. The observational error covariance matrix R is difficult to quantify, as this is related to both the errors in the satellite fluxgate magnetometers making the measurements, as well as “representativeness error,” which is the error introduced when trying to fit a finite number of PC modes to the data, which may not be capable of representing the true field, especially since our PC modes do not model poloidal current sources flowing at satellite altitude. Although these errors of representation are expected to be correlated among nearby measurement points, we have little information about the structure of these, or for that matter, other data errors. We thus make the assumption that data errors are uncorrelated with constant variance and express the covariance matrix simply as $R = \sigma^2 I$ for some unspecified variance σ^2 . A judicious choice of σ^2 can help offset the influence of these poorly characterized correlations on the OI fit. With this substitution, the problem is now to solve

$$\min_{\alpha} \frac{1}{\sigma^2} \|\mathbf{y}_{\text{obs}} - H\alpha\|^2 + \left\| \tilde{C}^{-\frac{1}{2}} \alpha \right\|^2. \quad (18)$$

This is equivalent to the minimization problem

$$\min_{\alpha} \|\mathbf{y}_{\text{obs}} - H\alpha\|^2 + \sigma^2 \left\| \tilde{C}^{-\frac{1}{2}} \alpha \right\|^2, \quad (19)$$

which is now expressed as a Tikhonov regularization problem [Hansen, 1998]. From this expression we see that σ^2 acts as a regularization parameter which determines a trade-off between minimizing the norm of the residuals $\|\mathbf{y}_{\text{obs}} - H\alpha\|$ and the norm of the solution term $\|\tilde{C}^{-1/2} \alpha\|$. The solution of this minimization problem can be found by solving the least squares system:

$$\begin{pmatrix} H \\ \sigma \tilde{C}^{-\frac{1}{2}} \end{pmatrix} \alpha = \begin{pmatrix} \mathbf{y}_{\text{obs}} \\ 0 \end{pmatrix}. \quad (20)$$

In theory the parameter σ should come from some deeper knowledge about the observational error or model omission error. However, since we do not have a full understanding of the observational error covariance, in this study we will choose σ to obtain a reasonable trade-off between minimizing the residuals and the solution norm. In practice, we find that choosing σ as the value corresponding to the corner of the L-curve [Hansen and O’Leary, 1993] achieves this goal.

2.2. The 2-D SECS

By applying the Helmholtz theorem, Amm [1997] showed that the ionospheric current density can be uniquely decomposed into a superposition of divergence-free and curl-free elementary systems, defined as

$$\mathbf{J}_{2-D,df}(r', \theta', \phi') = \frac{I_{2-D,df}}{4\pi b} \delta(r' - b) \cot\left(\frac{\theta'}{2}\right) \hat{\mathbf{e}}_{\phi'} \quad (21)$$

$$\mathbf{J}_{2-D,cf}(r', \theta', \phi') = \frac{I_{2-D,cf}}{4\pi b} \delta(r' - b) \cot\left(\frac{\theta'}{2}\right) \hat{\mathbf{e}}_{\theta'}. \quad (22)$$

Here the coordinates (θ', ϕ') define a pole location about which the elementary system is axially symmetric [see Amm and Viljanen, 1999, Figure 1]. The parameter b defines the radius of the shell on which the currents flow, in this paper taken to be $b = R + 110$ km. The unit vectors, $\hat{\mathbf{e}}_{\theta'}$, $\hat{\mathbf{e}}_{\phi'}$ are the standard basis vectors of a

spherical coordinate system which has its North Pole at location (θ', ϕ') . Finally, $I_{2-D,df}$ and $I_{2-D,cf}$ are scaling factors representing the strength of each elementary system, to be determined by fitting magnetic measurements. Expressions for the magnetic field due to the elementary current systems are omitted here, but the divergence-free 2-D SECS field equations may be found in *Amm and Viljanen* [1999], and the curl-free 2-D SECS field equations can be calculated using Ampere's law as in *Juusola et al.* [2006].

The 2-D SECS method has a number of attractive properties for fitting magnetic perturbations originating in the ionosphere observed by satellites and ground observatories. First, the expressions for the currents and magnetic fields are naturally expressed in spherical coordinates and so they automatically account for the Earth's spherical geometry. Second, because they form a complete set for 2-D vector fields on the sphere, no a priori assumptions are required regarding the direction of current flow. These two properties make SECS an attractive alternative to line current methods. Third, SECS is a local method, so if data are only available from a localized region, even if irregularly shaped, the method can be applied by defining SECS poles covering the data region. Fourth, due to the relatively simple expressions for the SECS magnetic fields, they are straightforward to implement in a least squares analysis using satellite or ground observations.

One of the main difficulties in using 2-D SECS to interpret ionospheric current systems is that it is often necessary to allow for a large number of elementary systems to adequately cover the data region and represent the spatially complex current flow patterns. This typically leads to a highly ill posed least squares problem, requiring heavy regularization to prevent large and nonphysical current flow solutions. Therefore, the resulting model may explain the observations well but can deteriorate rapidly in accuracy as we move away from the data region.

In order to fit the 2-D SECS model to the satellite measurements, we again form a Tikhonov regularization problem by solving

$$\min_{\mathbf{x}} \|\mathbf{y}_{\text{obs}} - \mathbf{A}\mathbf{x}\|^2 + \lambda^2 \|\mathbf{x}\|^2. \quad (23)$$

Here \mathbf{x} is a vector of the divergence-free amplitudes $I_{2-D,df}$, \mathbf{A} is the matrix relating the 2-D SECS parameters to the magnetic field data, and λ is a damping parameter. In this study we will not fit the curl-free 2-D SECS to the Swarm data, as we are primarily interested in toroidal flow in the low- and middle-latitude E region. Since we do not have knowledge of the model error covariance matrix in this case, we simply minimize the solution norm $\|\mathbf{x}\|$ to prevent nonphysically large 2-D SECS amplitudes in the solution. The damping parameter λ is again chosen using L-curve analysis.

2.3. The 1-D SECS

A one-dimensional variant of the SECS method was developed by *Vanhamäki et al.* [2003] by assuming vanishing longitudinal gradients of the currents. This results in a new set of basis functions which depend only on latitude, suitable for fitting data from a north-south chain of ground observatories [*Vanhamäki et al.*, 2003] or a single polar orbiting magnetic satellite mission such as CHAMP [*Juusola et al.*, 2006]. The 1-D elementary current systems are given by

$$\mathbf{J}_{1-D,df}(\theta, \theta_0) = \frac{I_{1-D,df}}{2b} \hat{\mathbf{e}}_\phi \begin{cases} -\tan\left(\frac{\theta}{2}\right), & \theta < \theta_0 \\ \cot\left(\frac{\theta}{2}\right), & \theta > \theta_0 \end{cases} \quad (24)$$

$$\mathbf{J}_{1-D,cf}(\theta, \theta_0) = \frac{I_{1-D,cf}}{2b} \hat{\mathbf{e}}_\theta \begin{cases} -\tan\left(\frac{\theta}{2}\right), & \theta < \theta_0 \\ \cot\left(\frac{\theta}{2}\right), & \theta > \theta_0 \end{cases} \quad (25)$$

$$\mathbf{J}_{1-D,\parallel}(r, \theta, \theta_0) = \hat{\mathbf{e}}_r \begin{cases} \frac{I_{1-D,cf}}{r^2} \left(\frac{1}{2} - \frac{\delta(\theta - \theta_0)}{\sin \theta_0} \right), & r \geq b \\ 0, & r < b \end{cases}, \quad (26)$$

where θ_0 is the colatitude defining the pole of the 1-D elementary system. The divergence-free 1-D SECS flow zonally and change their flow direction at the pole colatitude θ_0 [see *Juusola et al.*, 2006, Figure 2]. The curl-free 1-D SECS flow meridionally either toward or away from the pole colatitude θ_0 , while the FAC 1-D SECS allow for a vertical sheet current at the colatitude θ_0 . Expressions for the magnetic field vector are again omitted but may be found in *Vanhamäki et al.* [2003] and *Juusola et al.* [2006]. Due to the assumption of vanishing

longitude gradients, the 1-D SECS are suitable for analyzing electrojet-type currents and have been used to study the polar electrojets [Vanhamäki *et al.*, 2003].

In this paper, we will apply the 1-D SECS method to analyze low-latitude daytime measurements from single Swarm satellites, which include prominent signatures of the equatorial electrojet. The resulting east-west current flow profiles will be compared with single satellite PCA fits in section 3.

Similarly to the 2-D SECS case, to fit the 1-D SECS, we solve the regularized least squares problem:

$$\min_{\mathbf{x}} \|\mathbf{y}_{\text{obs}} - A\mathbf{x}\|^2 + \lambda^2 \|\mathbf{L}\mathbf{x}\|^2. \quad (27)$$

Here \mathbf{x} is a vector of the 1-D SECS amplitudes $I_{1-D,df}$ and $I_{1-D,cf}$, A is the matrix relating these amplitudes to the magnetic field observations, and L is a regularization matrix, chosen as the second-order finite difference operator:

$$L = \begin{pmatrix} 1 & -2 & 1 & & \\ & \ddots & \ddots & \ddots & \\ & & & 1 & -2 & 1 \end{pmatrix}. \quad (28)$$

Since the 1-D SECS elementary currents are aligned along a meridian, this regularization helps to generate a smooth transition from one elementary current system to its neighbor, preventing large nonphysical oscillations in the amplitudes between neighboring systems. We choose λ as the corner of the L-curve for each fit.

3. Results

Here we present results from applying the SECS and PCA methods to recover equivalent current flow from Swarm data, using both single satellite and multisatellite fits. In all cases, the Swarm data were preprocessed using the following steps. First, the data were separated into half orbital tracks, covering the North to South Pole. Only vector measurements with at least two operational star cameras were used in order to obtain an accurate measurement in the north-east-center (NEC) frame, a condition which was satisfied about 99.6% of the time for each satellite. Next, we computed along-track root-mean-square (RMS) differences with a main field model [Alken *et al.*, 2015] in each vector component in order to detect and discard tracks with abnormally large values which could be due to miscalibrations during satellite maneuvers, instrument noise, or possible large disturbances from magnetospheric currents. About 5% of tracks for each satellite were discarded due to this procedure. Finally, we restrict our analysis to geomagnetically quiet periods and only keep tracks with a Kp value less than 2o, a condition which was satisfied about 57% of the time. We will extend our PCA methodology to more active times, including geomagnetic storm events, in a future study.

Since we are focusing only on ionospheric currents in this study, next we removed core, crustal, and magnetospheric field models from the Swarm data. The core field model was built using the methodology described in Alken *et al.* [2015]. For the crustal field we used MF7 [Maus *et al.*, 2008] and for the magnetospheric field model we used POMME [Maus and Lühr, 2005; Lühr and Maus, 2010]. The POMME external field model is parameterized by the Dst index, which is known to contain baseline jumps and does not always accurately reflect the strength of the magnetospheric ring current [Lühr *et al.*, 2016]. Therefore, we also fit an external degree 1 spherical harmonic model, aligned with the Earth's magnetic dipole axis to each track, to help remove any residual ring current field. In this study we focus only on low- and middle-latitude ionospheric current systems, and so when applying the SECS and PCA models, we fit only data below 40° quasi-dipole latitude.

3.1. Single Satellite

We applied the 1-D SECS and PCA models to fit low- and middle-latitude measurements from each individual Swarm satellite. For the 1-D SECS approach, we defined poles spanning 60°S to 60°N with a spacing of 0.5° geocentric latitude. This latitude range is sufficient to cover the 40°S to 40°N QD latitude range used for the data fitting at all longitudes, leaving additional room to avoid edge effects. This resulted in a total of 241 pole locations for each satellite track. We used only divergence-free 1-D SECS in the analysis, and so there were a total of 241 parameters in the 1-D SECS model. For the PCA approach, we found that 10 modes were adequate to obtain a good fit to the data, and so we had a total of 10 parameters for the PCA model.

An example profile from Swarm A along with the 1-D SECS and PCA fits is shown in Figure 6. This profile was measured on 1 January 2015 when the satellite was in a local time of 14:24. At this time of day we expect a

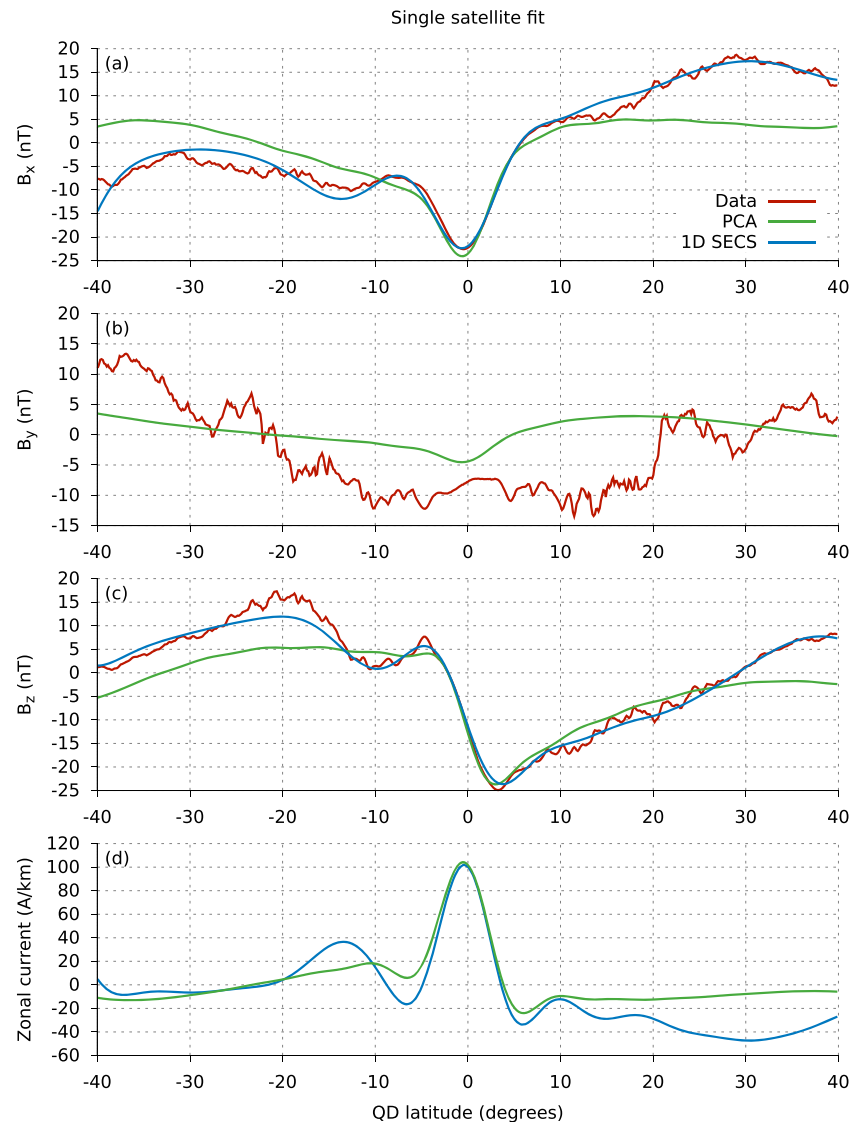


Figure 6. Single track profile recorded by Swarm A around 05 UT on 1 January 2015 (14:24 local time). (a)–(c) Magnetic vector measurements are shown in red for B_x , B_y , and B_z components. Modeled magnetic field components are shown in green for PCA method and blue for 1-D SECS method. Note that the 1-D SECS model does not give a prediction for B_y since we use only divergence-free elementary systems. (d) The equivalent zonal current in green for the PCA fit and blue for the 1-D SECS fit. Positive (negative) current corresponds to eastward (westward) flow.

prominent Sq and equatorial electrojet current system, and indeed, we see the characteristic EEJ peak at low latitudes in the B_x component and a sign change in the B_z component. In Figures 6a–6c, the red curves show the Swarm vector magnetic field measurements, the green curves show the resulting fit from the PCA method, and the blue curves show the fit from the 1-D SECS method. In both cases we find a good fit to the data, in particular, in the EEJ region in the B_x and B_z components. For the B_y component, the 1-D SECS approach does not provide a prediction, since we are fitting only divergence-free elementary systems, which do not affect the B_y component. For the PCA method, we find that the magnetic component fits follow the general trend of the data but do not model the small-scale features. This is particularly true for the B_y component. At low and midlatitudes, the observed B_y component is affected primarily from F region interhemispheric field-aligned currents, gravity and pressure gradient current, and vertical and meridional current flow from the EEJ system. These currents are all flowing at satellite altitude, but our PCA approach is only modeling toroidal currents on a shell at 110 km altitude, and so is unable to fit these poloidal current systems. The east-west component of the fitted equivalent current is plotted in blue in Figure 6d. For both methods we find a strong peak at the equator,

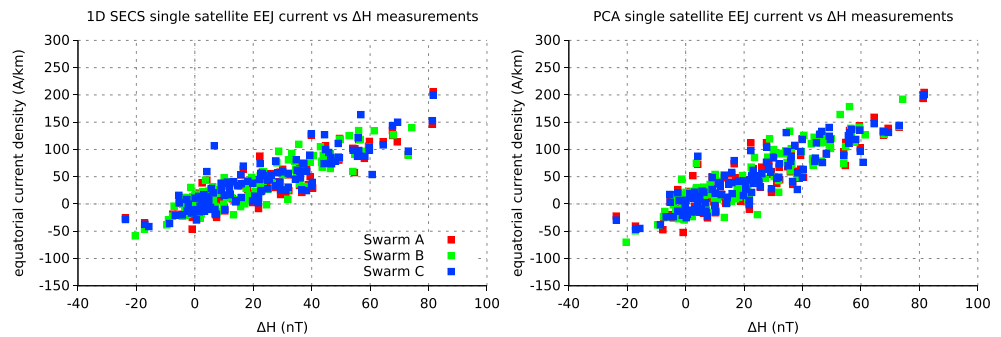


Figure 7. Comparison of SAM-MBO ΔH observations with eastward current on the magnetic equator, recovered from single satellite (left) 1-D SECS approach and (right) PCA approach.

representing eastward EEJ current flow, as well as reduced current at $\pm 5^\circ$ QD latitude, indicating effects of F region winds [Fambitakoye *et al.*, 1976]. Both methods predict a peak EEJ strength of about 100 A/km for this orbit.

In order to investigate the quality of the computed currents from both methods, we compared the prediction of J_ϕ on the magnetic equator with observations from two ground observatories in West Africa. One of the observatories, Samogossani (SAM, 0.18° N dip latitude, 11.60° N, 5.77° W, 351 m), is located under the dip equator and is able to track variations due to the equatorial electrojet current. The other, Mbour (MBO, 3.23° dip latitude, 14.39° N, 16.96° W, 7 m), is part of the INTERMAGNET network. MBO is farther from the dip equator and is less affected by the EEJ currents. Taking the difference SAM-MBO in the horizontal field component, denoted ΔH , filters out much of the Sq variation leaving the EEJ signal intact [Rastogi and Klobuchar, 1990; Anderson *et al.*, 2004]. We used all observatory measurements from November 2013 to February 2015. To define a simultaneous measurement event, we require that the satellite cross the magnetic equator within 5 min of a SAM measurement and within a 10° longitude window centered at SAM's location. We consider only data collected between 06 and 18 local time, due to the weak EEJ signal during nighttime. The results are shown in Figure 7. For both methods, we find correlations of about 90% between the peak EEJ current and ΔH observations for all satellites. Table 1 displays the correlation values from each satellite fit. The table indicates that the PCA and 1-D SECS approaches work equally well in estimating the peak EEJ current for the single satellite case.

3.2. Multisatellite

The 2-D SECS and PCA methods are both well suited for analyzing measurements from multiple observation platforms, such as the three satellite Swarm constellation and/or ground observatory networks. In this section we will discuss results from fitting the 2-D SECS and PCA models to data from two or more Swarm satellites. First, we consider two constellation events when all three Swarm satellites crossed the magnetic equator within 5 min of each other. For these events, we list the date, longitude, local time, and UTC time of the magnetic equator crossing for each satellite in Table 2. Both events occurred during daytime, when Sq and EEJ currents are the dominant sources in the magnetic observations at low and middle latitudes. We fit the 2-D SECS and PCA models using data from all three satellites for these two events in order to investigate the

Table 1. Table of Correlations Between SAM-MBO ΔH Measurements and Satellite-Derived J_ϕ on the Magnetic Equator^a

| Satellite | N | 1-D SECS | PCA |
|-----------|-----|----------|------|
| Swarm A | 127 | 0.90 | 0.90 |
| Swarm B | 122 | 0.90 | 0.90 |
| Swarm C | 127 | 0.87 | 0.90 |

^aThe column labeled N contains the number of events used to calculate the correlation.

Table 2. Events Occurring on 18 January 2015 and 18 March 2016 When All Three Swarm Satellites Crossed the Magnetic Equator Within 5 min of Each Other^a

| Date | Satellite | Longitude | Local Time | UTC Time |
|-----------------|-----------|-----------|------------|----------|
| 18 January 2015 | Swarm A | 46.0° W | 12:49:44 | 15:53:49 |
| | Swarm C | 44.6° W | 12:55:21 | 15:53:41 |
| | Swarm B | 26.4° W | 14:12:36 | 15:58:07 |
| 18 March 2016 | Swarm A | 10.5° W | 10:39:25 | 11:21:37 |
| | Swarm C | 9.1° W | 10:45:03 | 11:21:33 |
| | Swarm B | 36.1° E | 13:50:37 | 11:26:24 |

^aThe table lists the longitude, local time, and UTC time when each satellite crossed the magnetic equator.

large-scale Sq and EEJ current structure. For the 2-D SECS approach, we define a uniform grid of poles spanning 60°S to 60°N in latitude with a spacing of 2°. In the zonal direction, we define a grid from the longitude of the Swarm A crossing to the Swarm B crossing with a buffer of 2° on each side to avoid edge effects. For the 18 January 2015 event, the range was 48°W to 24.4°W and for the 18 March 2016 event it was 12.5°W to 38.1°E. In both cases we use a longitude grid spacing of 3°. For the 18 January 2015 event, this configuration corresponds to 8 grid points in longitude and 61 grid points in latitude, for a total of 488 poles. For the 18 March 2016 event, we have 17 poles in longitude and 61 poles in latitude, for a total of 1037 poles. For this study, we fit only the divergence-free 2-D elementary systems, since we are mainly interested in the toroidal E region currents, and so the number of poles is equal to the number of model parameters for the 2-D SECS model. For the PCA approach, we use 10 modes for both fits, and so have 10 parameters in the PCA model. Figure 8 shows the results for fitting the 18 January 2015 event, when the longitude separation between Swarm A and B was about 19.6°. Figure 8a shows the vector magnetic field measurements from each Swarm satellite in red, along with the fit from the PCA model in green, and the 2-D SECS model in blue. Figure 8b shows the equivalent current system from the 2-D SECS model (left) and PCA model (right). For the 2-D SECS model, due to the large number of model parameters and limited satellite data, we had to impose heavier regularization to constrain the solution. This can be seen in Figure 8a where the SECS fit does not capture the sharp EEJ features at low latitudes in the B_x and B_z components due to the damping. In both equivalent current maps, we see current vortices which exhibit counterclockwise flow in the Northern Hemisphere and clockwise flow in the Southern Hemisphere. This is what we expect from a nominal daytime Sq system. However, in this particular event the Swarm constellation is flying in the South American sector, where the magnetic equator dips south. Each of the PCA basis functions have this geometry built in, and so the PCA solution nicely reproduces that feature in the current map. The 2-D SECS model has no information about the geomagnetic geometry and so cannot reproduce these low-latitude features based on the limited data available from the three satellites. Also, due to the heavier regularization required, the low-latitude 2-D SECS current contours are spaced farther apart, unable to capture the localized EEJ current flow. Figure 9 shows the results from fitting the second event on 18 March 2016 in the same format as Figure 8. For this event, the longitude spacing between Swarm A and B is about 46.6°, requiring more SECS poles to cover the larger data region and therefore more model parameters. Because of this, we imposed even more regularization to constrain the current solution. This can be seen in Figure 9a where the SECS fit not modeling well the low-latitude EEJ features. The equivalent current maps from both models again show the Northern and Southern Hemisphere vortices, but the PCA map shows more realistic enhanced current flow in the EEJ region.

Ultimately, when developing a new method of modeling ionospheric current sources, we would like to know how well it can predict magnetic fields in areas not used in the model fitting. To investigate this, we fit both the 2-D SECS and PCA models to the Swarm lower pair (A and C) and used the resulting model to predict the field at Swarm B's location. Since the orbital plane of Swarm B is slowly drifting away from A and C, this enables us to visualize the quality of the model predictions as a function of longitudinal separation. For this comparison, we used all Swarm data from the beginning of the mission until the end of 2016 and searched for events where all three satellites were in local times between 06 and 18 and crossed the magnetic equator within 5 min of each other. When such an event was found, we fit models to the Swarm A/C data only and then calculated the

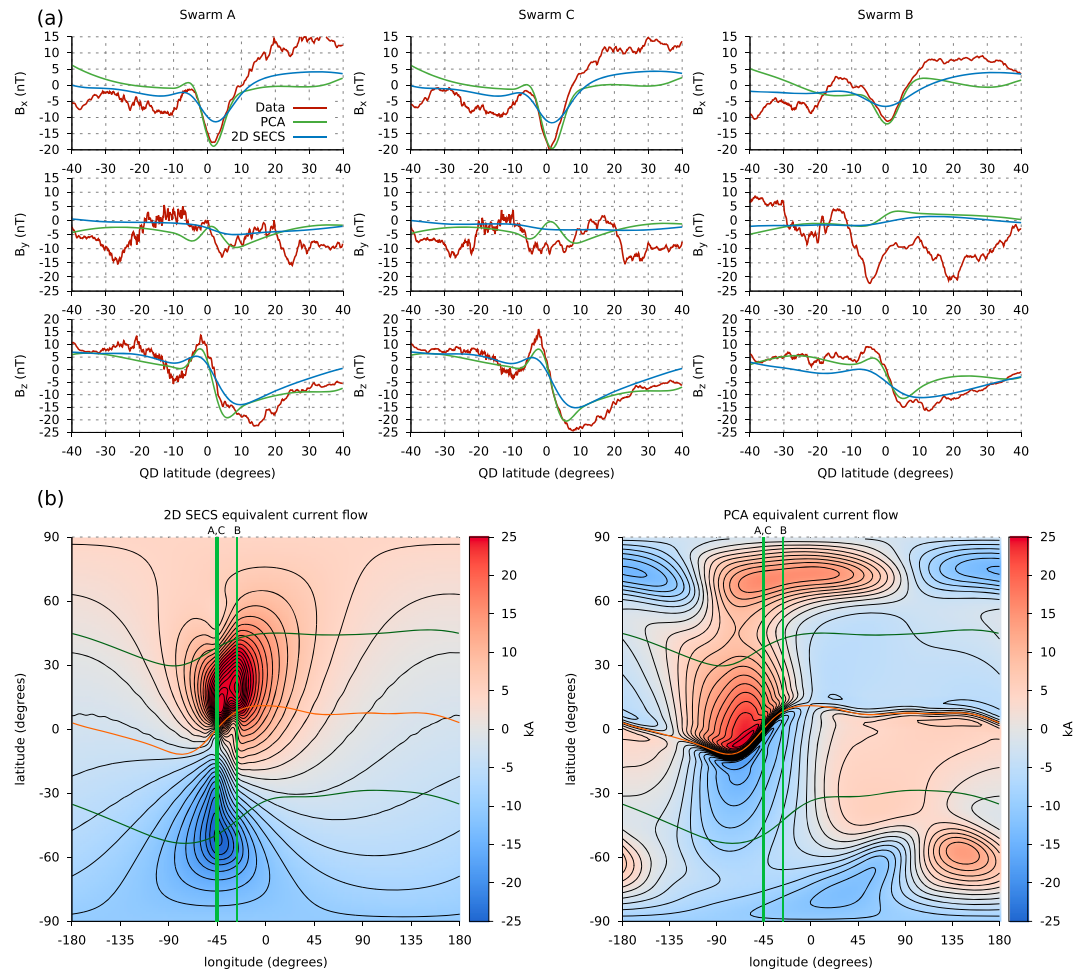


Figure 8. Magnetic field fits and corresponding current flow estimated from Swarm constellation event on 18 January 2015. (a) Vector magnetic field data recorded by each Swarm satellite (red), fit from PCA model (green) and fit from 2-D SECS model (blue). (b) Equivalent current flow at 110 km altitude from 2-D SECS (left) and PCA (right). Satellite tracks are shown in light green. Curves of constant QD latitude of $\pm 40^\circ$ at 110 km altitude shown in dark green. Magnetic equator at 110 km altitude is shown in orange. Contour spacing is 2 kA.

RMS difference between the Swarm B vector magnetic measurements and the model from 40°S to 40°N QD latitude. For the PCA approach, we used 10 modes to fit all models. For the 2-D SECS approach, the number of model parameters depended on the longitudinal separation of Swarm A and B. We used a constant 61 grid points in latitude spaced 2° apart from 60°S to 60°N . For longitude, we used a fixed grid spacing of 3° , which led to an increasing number of grid locations (and therefore model parameters) as the orbital plane of Swarm B separated farther from Swarm A. As before, the PCA fit used the optimal interpolation technique with the model error covariance matrix, while the 2-D SECS fit used a minimum-norm Tikhonov regularization. Both model fitting procedures used L-curve analysis to determine the regularization parameter.

The results are shown in Figure 10. For each model fit, we obtain a single RMS value for each of the vector magnetic field components measured by Swarm B. These are shown as red dots for the 2-D SECS models and blue dots for the PCA models. The solid lines represent the mean RMS as a function of longitudinal separation of Swarm A and B for the 2-D SECS (red) and PCA (blue) methods. For reference, the solid orange curve shows the RMS of the Swarm B measurement plotted as function of $\Delta\phi$ (i.e., if we were using a zero field prediction). The oscillations in the figure are due to the B satellite entering early morning local times (around 0700), when the low-latitude EEJ signal becomes weak due to the transition from a westward counter-electrojet to and eastward electrojet. This weaker signal is easier to model for both methods, resulting in lower RMS during

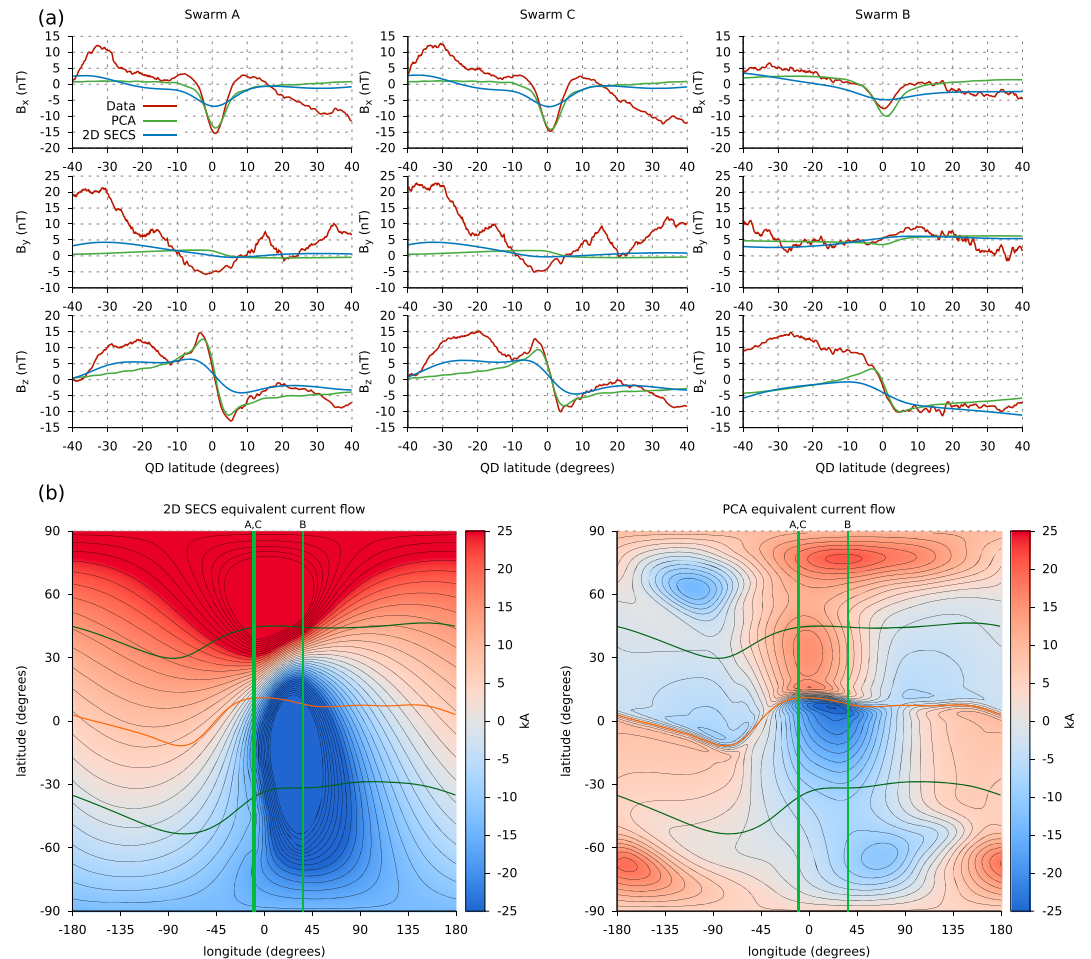


Figure 9. Magnetic field fits and corresponding current flow estimated from Swarm constellation event on 18 March 2016. (a) Vector magnetic field data recorded by each Swarm satellite (red), fit from PCA model (green) and fit from 2-D SECS model (blue). (b) Equivalent current flow at 110 km altitude from 2-D SECS (left) and PCA (right). Satellite tracks are shown in light green. Curves of constant QD latitude of $\pm 40^\circ$ at 110 km altitude shown in dark green. Magnetic equator at 110 km altitude is shown in orange. Contour spacing is 2 kA.

these periods. In the B_x component, both models produce RMS differences of less than 5 nT at small longitudinal separations (less than 3°). After about 5° separation, the 2-D SECS model performs worse than the null solution, while the PCA model performs slightly better up to about 20° separation. For the B_z component, the PCA model gives a better prediction (lower RMS) than 2-D SECS up to about 13° separation where it starts performing similarly to the null prediction. The 2-D SECS model RMS crosses the null prediction curve at around 4° separation. For the B_y component, the PCA model does not perform better than the null solution at any longitudinal separation, while the 2-D SECS model has lower RMS up to about 8° separation. As discussed previously, the B_y component contains many poloidal ionospheric current signatures which are not modeled by our current PCA approach, which likely explains the poor prediction in this component. Since we only fit divergence-free 2-D SECS, this model is also not fitting the poloidal sources contributing to B_y , but it is possible that the better fit at smaller longitudinal separations is due to the larger number of model parameters in the 2-D SECS model, which could absorb some of this signal even though it is not directly modeled with the curl-free elementary currents. Overall, we believe that this figure shows that our PCA approach is a promising method for predicting ionospheric field effects far away from data regions. We also note that the 2-D SECS method is not designed to predict realistic currents far away from the data region, as it is based on purely generic basis function expansions, so the analysis of Figure 10 is intended only to demonstrate the utility of the PCA approach for this purpose.

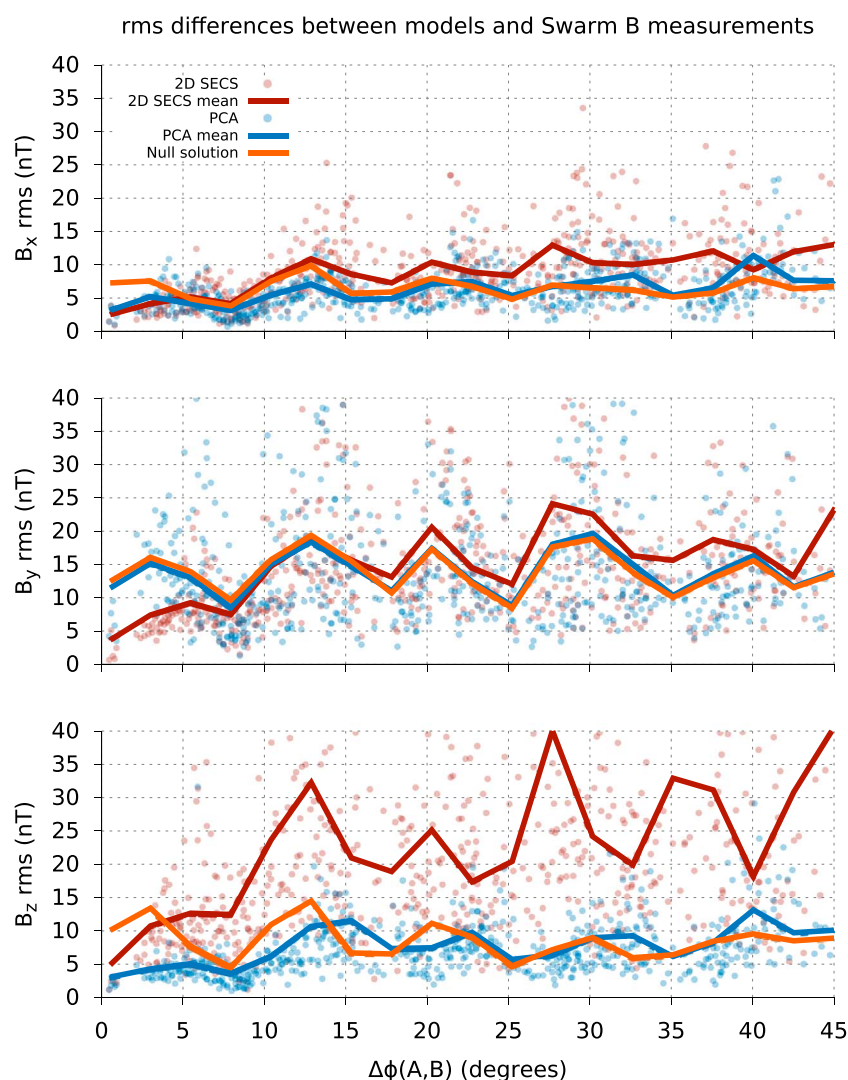


Figure 10. Vector RMS differences between Swarm B measurements and models predicted from Swarm A and C data as a function of longitude separation between A and B orbital planes. The 2-D SECS RMS values shown as red dots with the mean as a solid red line. PCA RMS values shown as blue dots with the mean as a solid blue line. Mean prediction using a zero field is shown in orange.

4. Conclusion

We have presented a new approach of combining TIEGCM physics-based ionospheric electrodynamics modeling with principal component analysis in order to interpret ionospheric signals observed by Swarm satellites. We applied this method to fitting data from both single satellite and multisatellite constellation data and found that the method was able to predict realistic equivalent current flow at *E* region altitudes, by validating against independent data. In the single satellite case, we compared the PCA-derived and 1-D SECS-derived current at low latitudes with ground observatory ΔH measurements and found about a 90% correlation for both methods. For the multisatellite case, we believe that this new PCA approach offers a significant step forward over other modeling methods. By fitting data from all three Swarm satellites, we found that the PCA model could reproduce realistic equivalent current flow using as few as 10 modes. Since we calculated independent modes for each universal time hour, ionospheric day/night differences were accounted for and so the spatial separation of the satellites had no influence on the number of modes required to model the large-scale low- and middle-latitude current system. The sharp EEJ features at low latitudes were well reproduced as well as the larger-scale *S_q* current flow at midlatitudes. We found that these features were not easily recovered using the 2-D SECS method, in part due to the large number of model parameters required for large spatial

separation of the data sources but also because the SECS basis functions contain no information about the ionospheric source geometries which are strongly aligned with the geomagnetic field. These geometries are naturally built in to the PCA basis functions due to the TIEGCM modeling. By fitting PCA models to the Swarm lower pair (A and C) and then using the model to predict the field at Swarm B, we found that the PCA approach can provide meaningful information about the ionospheric current system far away from the data region.

The present study was based on a TIEGCM run in 2009 under solar minimum conditions and also analyzed only equivalent current flow on a thin shell in the E region. Therefore, the resulting principal component modes are suitable only for quiet time studies of E region currents like Sq , EEJ , and PEJ . Future advancements of this work will include analysis of model runs during more active periods, including storm conditions, and make use of the full 3-D current output of TIEGCM in order to study poloidal current systems in the ionosphere, such as pressure-gradient currents, FAC, IHFAC, and EEJ meridional currents.

Acknowledgments

P. Coisson processed the ground observatory data used in this study. This work was supported by National Science Foundation grants EAR-1447036 and AGS-1135446. The National Center for Atmospheric Research is sponsored by the National Science Foundation. We gratefully acknowledge the European Space Agency for providing Swarm data, which is available from <https://earth.esa.int/web/guest/swarm/data-access> following registration. The ground observatory data used in this study can be obtained from the Bureau Central de Magnétisme Terrestre (<http://www.bcmf.fr>) and INTERMAGNET (<http://www.intermagnet.org>). The TIEGCM runs used in this work are available upon request.

References

- Aakjær, C. D., N. Olsen, and C. C. Finlay (2016), Determining polar ionospheric electrojet currents from Swarm satellite constellation magnetic data, *Earth Planets Space*, 68(1), 140, doi:10.1186/s40623-016-0509-y.
- Alken, P. (2016), Observations and modeling of the ionospheric gravity and diamagnetic current systems from CHAMP and Swarm measurements, *J. Geophys. Res. Space Physics*, 121, 589–601, doi:10.1002/2015JA022163.
- Alken, P., and S. Maus (2007), Spatio-temporal characterization of the equatorial electrojet from CHAMP, Ørsted, and SAC-C satellite magnetic measurements, *J. Geophys. Res.*, 112, A09305, doi:10.1029/2007JA012524.
- Alken, P., S. Maus, P. Vigneron, O. Sirol, and G. Hulot (2013), Swarm SCARF equatorial electric field inversion chain, *Earth Planets Space*, 65, 1309–1317, doi:10.5047/eps.2013.09.008.
- Alken, P., S. Maus, A. Chulliat, P. Vigneron, O. Sirol, and G. Hulot (2014), Swarm equatorial electric field chain: first results, *Geophys. Res. Lett.*, 42, 673–680, doi:10.1002/2014GL062658.
- Alken, P., S. Maus, A. Chulliat, and C. Manoj (2015), NOAA/NGDC candidate models for the 12th generation international geomagnetic reference field, *Earth Planets Space*, 67, 68, doi:10.1186/s40623-015-0215-1.
- Alken, P., A. Maute, and A. D. Richmond (2016), The F -region gravity and pressure gradient current systems: A review, *Space Sci. Rev.*, 206(1–4), 451–469, doi:10.1007/s11214-016-0266-z.
- Amm, O. (1997), Ionospheric elementary current systems in spherical coordinates and their application, *J. Geomag. Geoelectr.*, 49(7), 947–955.
- Amm, O., and A. Viljanen (1999), Ionospheric disturbance magnetic field continuation from the ground to the ionosphere using spherical elementary current systems, *Earth Planets Space*, 51(6), 431–440.
- Amm, O., H. Vanhamäki, K. Kauristie, C. Stolle, F. Christiansen, R. Haugmans, A. Masson, M. G. G. T. Taylor, R. Foberghagen, and C. P. Escoubet (2015), A method to derive maps of ionospheric conductances, currents, and convection from the Swarm multisatellite mission, *J. Geophys. Res. Space Physics*, 120, 3263–3282, doi:10.1002/2014JA020154.
- Anderson, D., A. Anghel, J. Chau, and O. Veliz (2004), Daytime vertical $E \times B$ drift velocities inferred from ground-based magnetometer observations at low latitudes, *Space Weather*, 2, S11001, doi:10.1029/2004SW000095.
- Chulliat, A., P. Vigneron, E. Thébault, O. Sirol, and G. Hulot (2013), Swarm SCARF dedicated ionospheric field inversion chain, *Earth Planets Space*, 65(11), 1271–1283.
- Chulliat, A., P. Vigneron, and G. Hulot (2016), First results from the Swarm dedicated ionospheric field inversion chain, *Earth Planets Space*, 68(1), 104.
- Cousins, E. D. P., T. Matsuo, and A. D. Richmond (2013), Mesoscale and large-scale variability in high-latitude ionospheric convection: Dominant modes and spatial/temporal coherence, *J. Geophys. Res. Space Physics*, 118, 7895–7904, doi:10.1002/2013JA019319.
- Cousins, E. D. P., T. Matsuo, and A. D. Richmond (2015), Mapping high-latitude ionospheric electrodynamics with SuperDARN and AMPERE, *J. Geophys. Res. Space Physics*, 120, 5854–5870, doi:10.1002/2014JA020463.
- Deguchi, R., H. Vanhamäki, H. Liu, and O. Amm (2013), Modification of one-dimensional spherical elementary current systems for applying at low/mid latitude. International Session, 2013.05.21.
- Egbert, G. D. (1997), Robust multiple-station magnetotelluric data processing, *Geophys. J. Int.*, 130(2), 475–496, doi:10.1111/j.1365-246X.1997.tb05663.x.
- Egbert, G. D., and J. R. Booker (1989), Multivariate analysis of geomagnetic array data: 1. The response space, *J. Geophys. Res.*, 94(B10), 14,227–14,247, doi:10.1029/JB094iB10p14227.
- Emery, B. A., R. G. Roble, E. C. Ridley, A. D. Richmond, D. J. Knipp, G. Crowley, D. S. Evans, F. J. Rich, and S. Maeda (2012), Parameterization of the ion convection and the auroral oval in the NCAR thermospheric general circulation models, NCAR Tech. Note NCAR/TN-491+STR, HAO/NCAR.
- Fambitakoye, O., P. N. Mayaud, and A. D. Richmond (1976), The equatorial electrojet and regular daily variation S_R :—III. Comparison of observations with a physical model, *J. Atmos. Terr. Phys.*, 38, 113–121.
- Forbes, J. M. (1981), The equatorial electrojet, *Rev. Geophys. Space Phys.*, 19(3), 469–504.
- Fratier, I., J.-M. Léger, F. Bertrand, T. Jager, G. Hulot, L. Brocco, and P. Vigneron (2016), Swarm absolute scalar magnetometers first in-orbit results, *Acta Astronaut.*, 121, 76–87, doi:10.1016/j.actaastro.2015.12.025.
- Friis-Christensen, E., H. Lühr, and G. Hulot (2006), Swarm: A constellation to study the Earth's magnetic field, *Earth Planets Space*, 58, 351–358.
- Haines, G. V. (1985), Spherical cap harmonic analysis, *J. Geophys. Res.*, 90(B3), 2583–2591, doi:10.1029/JB090iB03p02583.
- Haines, G. V., and J. M. Torta (1994), Determination of equivalent current sources from spherical cap harmonic models of geomagnetic field variations, *Geophys. J. Int.*, 118(3), 499–514, doi:10.1111/j.1365-246X.1994.tb03981.x.
- Hansen, P. (1998), *Rank-Deficient and Discrete Ill-Posed Problems: Numerical Aspects of Linear Inversion*, SIAM, Philadelphia, Pa.
- Hansen, P. C., and D. P. O'Leary (1993), The use of the L-curve in the regularization of discrete ill-posed problems, *SIAM J. Sci. Comput.*, 14(6), 1487–1503, doi:10.1137/0914086.

- Häusler, K., M. E. Hagan, J. M. Forbes, X. Zhang, E. Doornbos, S. Bruinsma, and G. Lu (2015), Intraannual variability of tides in the thermosphere from model simulations and in situ satellite observations, *J. Geophys. Res. Space Physics*, *120*, 751–765, doi:10.1002/2014JA020579.
- Heelis, R. A., J. K. Lowell, and R. W. Spiro (1982), A model of the high-latitude ionospheric convection pattern, *J. Geophys. Res.*, *87*(A8), 6339–6345, doi:10.1029/JA087iA08p06339.
- Jones, M., J. M. Forbes, and M. E. Hagan (2014), Tidal-induced net transport effects on the oxygen distribution in the thermosphere, *Geophys. Res. Lett.*, *41*, 5272–5279, doi:10.1002/2014GL060698.
- Juusola, L., O. Amm, and A. Viljanen (2006), One-dimensional spherical elementary current systems and their use for determining ionospheric currents from satellite measurements, *Earth Planets Space*, *58*(5), 667–678.
- Juusola, L., W. E. Archer, K. Kauristie, J. K. Burchill, H. Vanhamäki, and A. T. Aikio (2016), Ionospheric conductances and currents of a morning sector auroral arc from Swarm-A electric and magnetic field measurements, *Geophys. Res. Lett.*, *43*, 11,519–11,527, doi:10.1002/2016GL070248.
- Langel, R. A., M. Purucker, and M. Rajaram (1993), The equatorial electrojet and associated currents as seen in Magsat data, *J. Atmos. Terr. Phys.*, *55*, 1233–1269.
- Leger, J.-M., F. Bertrand, T. Jager, M. L. Prado, I. Fratter, and J.-C. Lalaurie (2009), Swarm absolute scalar and vector magnetometer based on helium 4 optical pumping, *Procedia Chem.*, *1*(1), 634–637, doi:10.1016/j.proche.2009.07.158.
- Lesur, V., M. Rother, I. Wardinski, R. Schachtschneider, M. Hamoudi, and A. Chambodut (2015), Parent magnetic field models for the IGRF-12: GFZ-candidates, *Earth Planets Space*, *67*(1), 87, doi:10.1186/s40623-015-0239-6.
- Lühr, H., and S. Maus (2010), Solar cycle dependence of quiet-time magnetospheric currents and a model of their near-Earth magnetic fields, *Earth Planets Space*, *62*, 843–848.
- Lühr, H., S. Maus, and M. Rother (2004), Noon-time equatorial electrojet: Its spatial features as determined by the CHAMP satellite, *J. Geophys. Res.*, *109*, A01306, doi:10.1029/2002JA009656.
- Lühr, H., C. Xiong, N. Olsen, and G. Le (2016), Near-Earth magnetic field effects of large-scale magnetospheric currents, *Space Sci. Rev.*, *206*(1), 521–545, doi:10.1007/s11214-016-0267-y.
- Matsuo, T., A. D. Richmond, and D. W. Nychka (2002), Modes of high-latitude electric field variability derived from DE-2 measurements: Empirical orthogonal function (EOF) analysis, *Geophys. Res. Lett.*, *29*(7), 11–1–11–4, doi:10.1029/2001GL014077.
- Matsuo, T., A. D. Richmond, and G. Lu (2005), Optimal interpolation analysis of high-latitude ionospheric electrodynamics using empirical orthogonal functions: Estimation of dominant modes of variability and temporal scales of large-scale electric fields, *J. Geophys. Res.*, *110*, A06301, doi:10.1029/2004JA010531.
- Maus, S., and H. Lühr (2005), Signature of the quiet-time magnetospheric magnetic field and its electromagnetic induction in the rotating Earth, *Geophys. J. Int.*, *162*, 755–763, doi:10.1111/j.1365-246X.2005.02691.x.
- Maus, S., F. Yin, H. Lühr, C. Manoj, M. Rother, J. Rauberg, I. Michaelis, C. Stolle, and R. D. Müller (2008), Resolution of direction of oceanic magnetic lineations by the sixth-generation lithospheric magnetic field model from CHAMP satellite magnetic measurements, *Geochem. Geophys. Geosyst.*, *9*, Q07021, doi:10.1029/2008GC001949.
- Maute, A. (2017), Thermosphere-Ionosphere-Electrodynamics General Circulation Model for the Ionospheric Connection Explorer: TIEGCM-ICON, *Space Sci. Rev.*, doi:10.1007/s11214-017-0330-3.
- Olsen, N. (1996), A new tool for determining ionospheric currents from magnetic satellite data, *Geophys. Res. Lett.*, *23*(24), 3635–3638, doi:10.1029/96GL02896.
- Olsen, N. (1997), Ionospheric *F* region currents at middle and low latitudes estimated from Magsat data, *J. Geophys. Res.*, *102*(A3), 4563–4576, doi:10.1029/96JA02949.
- Olsen, N., and C. Stolle (2016), Magnetic signatures of ionospheric and magnetospheric current systems during geomagnetic quiet conditions—An overview, *Space Sci. Rev.*, *206*(1–4), 5–25, doi:10.1007/s11214-016-0279-7.
- Pedatella, N. M., J. M. Forbes, and A. D. Richmond (2011), Seasonal and longitudinal variations of the solar quiet (*Sq*) current system during solar minimum determined by CHAMP satellite magnetic field observations, *J. Geophys. Res.*, *116*, A04317, doi:10.1029/2010JA016289.
- Pulkkinen, A., O. Amm, and A. Viljanen (2003), Ionospheric equivalent current distributions determined with the method of spherical elementary current systems, *J. Geophys. Res.*, *108*(A2), 1053, doi:10.1029/2001JA005085.
- Qian, L., A. G. Burns, B. A. Emery, B. Foster, G. Lu, A. Maute, A. D. Richmond, R. G. Roble, S. C. Solomon, and W. Wang (2014), The NCAR TIE-GCM, in *Modeling the Ionosphere-Thermosphere System*, edited by J. Huba, R. Schunk, and G. Khazanov, pp. 73–83, John Wiley, Ltd, Chichester, U. K., doi:10.1002/9781118704417.ch7.
- Rastogi, R. G., and J. A. Klobuchar (1990), Ionospheric electron content within the equatorial *F*₂ layer anomaly belt, *J. Geophys. Res.*, *95*, 19,045–19,052.
- Richmond, A. D. (1995), Ionospheric electrodynamics using magnetic apex coordinates, *J. Geomag. Geoelectr.*, *47*, 191–212.
- Richmond, A. D., and Y. Kamide (1988), Mapping electrodynamic features of the high-latitude ionosphere from localized observations: Technique, *J. Geophys. Res.*, *93*, 5741–5759, doi:10.1029/JA093iA06p05741.
- Richmond, A. D., and A. Maute (2014), Ionospheric Electrodynamics Modeling, in *Modeling the Ionosphere-Thermosphere System*, edited by J. Huba, R. Schunk, and G. Khazanov, pp. 57–71, John Wiley, Ltd, Chichester, U. K., doi:10.1002/9781118704417.ch6.
- Richmond, A. D., E. C. Ridley, and R. G. Roble (1992), A thermosphere/ionosphere general circulation model with coupled electrodynamics, *Geophys. Res. Lett.*, *6*, 601–604.
- Roble, R. G., R. E. Dickinson, and E. C. Ridley (1982), Global circulation and temperature structure of thermosphere with high-latitude plasma convection, *J. Geophys. Res.*, *87*(A3), 1599–1614, doi:10.1029/JA087iA03p01599.
- Roble, R. G., E. C. Ridley, A. D. Richmond, and R. E. Dickinson (1988), A coupled thermosphere/ionosphere general circulation model, *Geophys. Res. Lett.*, *15*, 1325–1328.
- Sabaka, T. J., N. Olsen, and M. E. Purucker (2004), Extending comprehensive models of the Earth's magnetic field with Ørsted and CHAMP data, *Geophys. J. Int.*, *159*, 521–547, doi:10.1111/j.1365-246X.2004.02421.x.
- Sabaka, T. J., L. Toffner-Clausen, and N. Olsen (2013), Use of the Comprehensive Inversion method for Swarm satellite data analysis, *Earth Planets Space*, *65*(11), 1201–1222.
- Smirnov, M. Y., and G. D. Egbert (2012), Robust principal component analysis of electromagnetic arrays with missing data, *Geophys. J. Int.*, *190*(3), 1423–1438, doi:10.1111/j.1365-246X.2012.05569.x.
- Sun, W., W.-Y. Xu, and S.-I. Akasofu (1998), Mathematical separation of directly driven and unloading components in the ionospheric equivalent currents during substorms, *J. Geophys. Res.*, *103*(A6), 11,695–11,700, doi:10.1029/97JA03458.
- Toffner-Clausen, L., V. Lesur, N. Olsen, and C. C. Finlay (2016), In-flight scalar calibration and characterisation of the Swarm magnetometry package, *Earth Planets Space*, *68*(1), 129, doi:10.1186/s40623-016-0501-6.

- Vanhamäki, H., O. Amm, and A. Viljanen (2003), One-dimensional upward continuation of the ground magnetic field disturbance using spherical elementary current systems, *Earth Planets Space*, *55*(10), 613–625.
- Vennerstrom, S., and T. Moretto (2013), Monitoring auroral electrojets with satellite data, *Space Weather*, *11*, 509–519, doi:10.1002/swe.20090.
- Waters, C. L., J. W. Gjerloev, M. Dupont, and R. J. Barnes (2015), Global maps of ground magnetometer data, *J. Geophys. Res. Space Physics*, *120*, 9651–9660, doi:10.1002/2015JA021596.
- Weimer, D. R. (2013), An empirical model of ground-level geomagnetic perturbations, *Space Weather*, *11*, 107–120, doi:10.1002/swe.20030.
- Weimer, D. R., C. R. Clauer, M. J. Engebretson, T. L. Hansen, H. Gleisner, I. Mann, and K. Yumoto (2010), Statistical maps of geomagnetic perturbations as a function of the interplanetary magnetic field, *J. Geophys. Res. Space Physics*, *115*, A10320, doi:10.1029/2010JA015540.
- Yamazaki, Y., and A. Maute (2016), *S_q* and *EEJ*—A review on the daily variation of the geomagnetic field caused by ionospheric dynamo currents, *Space Sci. Rev.*, *206*(1), 299–405, doi:10.1007/s11214-016-0282-z.
- Yamazaki, Y., et al. (2011), An empirical model of the quiet daily geomagnetic field variation, *J. Geophys. Res.*, *116*, A10312, doi:10.1029/2011JA016487.